# Fingering phenomena associated with insoluble surfactant spreading on thin liquid films

By M. R. E. WARNER[1], R. V. CRASTER[1] AND O. K. MATAR[2]

[1]Department of Mathematics, Imperial College London, South Kensington Campus,
London SW7 2AZ, UK

[2]Department of Chemical Engineering and Chemical Technology, Imperial College London, South
Kensington Campus, London SW7 2AZ, UK

We study the linear and nonlinear stability of a thick surfactant deposition spreading on a thin liquid film using transient growth analysis (TGA) and direct numerical simulations (DNS) of the two-dimensional lubrication equations, respectively. Results of the TGA of the one-dimensional spatially and temporally evolving base state reveal disturbance growth and the selection of a perturbation of intermediate wavenumber. This perturbation targets the 'contact region' between the deposition and the underlying thin liquid film and grows despite the absence of intermolecular forces. Increasing the initial thickness ratio of the deposition to the thin film and decreasing the relative magnitude of capillarity and surface diffusion further amplify perturbation growth. The DNS results clearly show the formation of fingers in the contact region behind the surfactant leading edge and provide further confirmation of the TGA findings.

## 1. Introduction

Spreading surfactant over the surface of thin liquid layers receives considerable attention in both the theoretical and experimental literature. Such spreading processes are of importance to numerous industrial, biomedical and daily life settings, including coating flow technology, micro-fluidics, surfactant replacement therapy for neonates, film drainage in emulsions and foams and drying of semi-conductor wafers in microelectronics (Leenaars, Huethorst & van Oekel 1990; Grotberg 1994; DeWitt, Gallez & Christov 1994; Braun, Snow & Pernisz 1999; Matar & Craster 2001). A fluid flow is primarily driven by surface tension gradients that arise due to non-uniformities in the surfactant interfacial concentration, that, in turn, give rise to so-called Marangoni stresses (Edwards, Brenner & Wasan 1991). These stresses drive rapid surfactant spreading in the direction of the uncontaminated (surfactant-free) liquid.

Numerous experimental and modelling studies have investigated the surfactant spreading process driven by Marangoni stresses, surface and bulk diffusion, gravity, capillarity, intermolecular forces and non-Newtonian effects in the absence of perturbations (Borgas & Grotberg 1988; Gaver & Grotberg 1990, 1992; Halpern & Grotberg 1992; Jensen & Grotberg 1992, 1993; Craster & Matar 2000; Schwartz & Roy 2001; Matar, Craster & Warner 2002; Warner, Craster & Matar 2002*a*, *b*). These studies have concluded that the spreading is accompanied by severe thinning of the film near the surfactant deposition region. This thinning occurs to balance the surface stress caused by the large surfactant concentration gradient in this region.
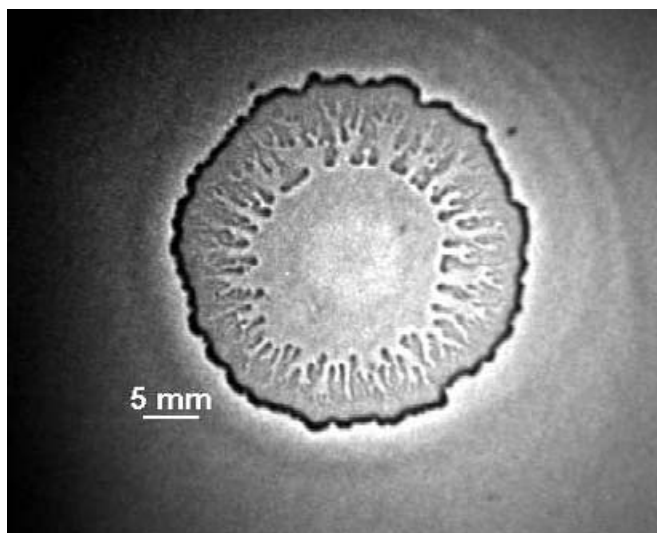
Figure 1. Fingering patterns generated 0.31 s following the deposition of a 9 μl droplet of 1.2 CMC SDS solution on a thin water film of approximate initial thickness 25 μm (Afsar-Siddiqui *et al.* 2003*b*).

Additionally, at the surfactant leading edge (where the surfactant-coated film meets the uncontaminated liquid layer) a thickened front is formed (Jensen & Grotberg 1992). In the presence of significant solubility effects, these features become accentuated: the front becomes more pulse-like, achieving peak values in excess of 3–4 times the undisturbed film height, while the thin region upstream becomes considerably more depressed (Jensen & Grotberg 1993). It has also been shown that the film in the thinning region can rapidly thin under the action of Marangoni stresses to achieve thicknesses of the order of 100 nm; for such values van der Waals forces become operative and induce film rupture in finite time.

In addition to this potential rupture instability, the spreading process is accompanied by another intriguing and striking instability that manifests itself via the formation of surfactant-coated fingers; an example of typical experimentally observed fingers is shown in figure 1. The lighter central region in figure 1 is the surfactant-laden droplet from which the fingers emanate. These fingers appear in the thinning region behind a crenelated advancing front (the dark outer contour in the figure). This instability has been observed in numerous articles: Marmur & Lelah (1981); Troian, Wu & Safran (1989); He & Ketterson (1995); Frank & Garoff (1995); Bardon *et al.* (1996); Cachile *et al.* (1999); Cachile & Cazabat (1999); Cachile *et al.* (2002); Afsar-Siddiqui, Luckham & Matar (2003*a, b*). The fingers undergo branching, coalescence and tip-splitting as they spread in the direction of uncontaminated liquid. This may give rise to non-uniform coating and could be undesirable in many applications.

Although the origin of the fingers has been much discussed, no conclusive and precise argument has yet appeared in the literature. Note that, in figure 1, we have chosen to present patterns associated with a soluble surfactant (SDS) for which the fingers are more pronounced and hence visualized more easily. Nonetheless, sparingly soluble surfactants such as AOT (see figure 2) also give rise to patterns, that, however, are somewhat less pronounced. Motivated by this latter picture we shall explore the instability mechanism not in axisymmetry, but for a planar geometry. We shall
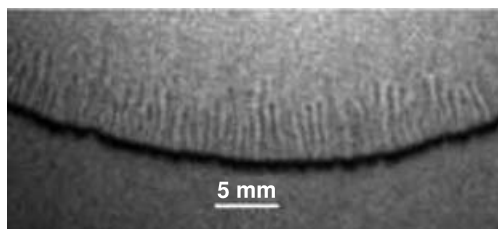
FIGURE 2. A close-up of the fingering patterns generated 5 s following the deposition of a 6 μl droplet of 1.6 CMC AOT solution on a thin water film of approximate initial thickness 25 μm (Afsar-Siddiqui *et al.* 2003*a*).

also ignore solubility and investigate whether a realistic destabilizing mechanism is deducible without recourse to solubility.

Troian, Herbohlzheimer & Safran (1990) first proposed a model that attempted to isolate the destabilizing mechanism using a linear stability analysis that exploited certain similarities between the present instability and viscous fingering (Saffman & Taylor 1958). Subsequently, in a series of articles, Matar & Troian (1997, 1998, 1999*a*, *b*) examined the stability of a surfactant monolayer spreading on a liquid film of dimensionless thickness equal to unity in the presence of Marangoni stresses, surface diffusion, capillarity and van der Waals forces using linear stability and transient growth analyses as well as direct numerical simulations of the fully nonlinear governing equations. Their results showed that sustained growth could only be obtained when van der Waals forces were significant; in the absence of these forces, large transient growth was obtained, ultimately followed by decay. This focus upon the monolayer leading edge, and constant thickness layers, appears to be the current direction of research into the finger origin. Recent work by Fischer & Troian (2003) revisits this type of analysis, and shows that growth followed by decay is once again obtained for the constant thickness layer, despite the use of an alternative measure of perturbation growth. At a slight tangent to this research is our article, Warner *et al.* (2002*b*), which conducted a systematic analysis of the linear and nonlinear stability of the van-der-Waals-driven rupture instability, which accompanies the spreading process and showed that a most dangerous 'mode' is selected that corresponds to an intermediate wavenumber. Those results, including three-dimensional reconstructions of the spreading film that exhibited finger-like protrusions in the thinning region, established van der Waals forces as a candidate mechanism for the instability.

Recent experimental studies (Cachile *et al.* 1999, 2002; Cachile & Cazabat 1999), however, have presented results that show fingering in regimes where significant van der Waals forces cannot be the mechanism. In particular, Cachile *et al.* (2002) rule out van der Waals forces as being an essential ingredient for unstable flow since they observe fingers even though the solvent used in that study initially wetted the underlying substrate perfectly. Additionally, Afsar-Siddiqui *et al.* (2003*a*, *b*) have studied the fingered spreading of AOT and SDS surfactants on water films resting on glass substrates, and have shown that the average finger wavelength is proportional to $H_b^{2/3}$, where $H_b$ is the undisturbed film thickness. This scaling is consistent with a Marangoni-driven rather than a van-der-Waals-driven fingering instability; the latter would have given rise to a $H_b^2$ scaling (Afsar-Siddiqui *et al.* 2003*a*, *b*). Therefore we conclude that although van der Waals forces may play a role for extremely thin fluid layers, their presence may otherwise not be necessary for instability and they will be neglected herein.

Motivated by these recent experimental studies, we re-examine the stability of the spreading process with the aim of determining the physical mechanism responsible for the fingering instability. Attention is focused on the spreading dynamics of surfactant deposited on an initially undisturbed film in the absence of van der Waals forces. The crucial difference between the present and previous studies is in the thickness of the undisturbed layer underlying the surfactant deposition. Whereas previous authors have chosen to examine the stability of a monolayer on a film of unity dimensionless thickness, in the present paper we consider a surfactant deposition of order-one thickness spreading over a film of much smaller thickness. We believe that this constitutes a faithful representation of the procedure utilized in the experimental studies; in reality, the disparity in thickness between the surfactant deposition and underlying film thickness is large. By conducting a transient growth analysis and full numerical simulations, we find that this disparity is essential for instability and finger formation: below a critical value, which depends on the remaining system parameters (such as a surface Péclet number and capillarity parameter), only transient growth is observed. This leads us naturally to the identification of the physical processes underlying the finger formation.

The rest of this paper is organized as follows. Section 2 presents the equations governing the dynamics of the base state and applied disturbances. In §3, we present a discussion of the results that includes a breakdown of the disturbance 'energy' in order to isolate the destabilizing mechanism. Finally, concluding remarks are provided in §4.

## 2. Formulation

In this section, we formulate the mathematical model that describes the dynamics of the spreading process. Details of this formulation have been provided elsewhere (Jensen & Grotberg 1992; Matar & Troian 1997, 1999$a$, $b$; Warner *et al.* 2002$b$), hence only the essential steps are given here.

### 2.1. *Governing equations and scaling*

We consider the spreading of a mound, or drop, of fluid of initial thickness $\mathscr{H}$ and extent $\mathscr{L}$, uniformly coated with insoluble surfactant of initial concentration, $\Gamma_m$. This deposition, bounded from above by an essentially inviscid gas (air), is deposited on an initially undisturbed film, of the same fluid, of thickness $\mathscr{H}_b$, resting on a horizontal, rigid and impermeable solid substrate, as shown in figure 3. This schematic represents a cross-section through the flow in the absence of the fingers. The strongly reduced surface tension at the drop edge drives a Marangoni flow characterized by a ramped structure with a sharp leading front; conservation of mass leads to severe thinning behind this ramped region. It is in this thinning region that the fingers emerge, apparently from the drop edge.

The fluid is assumed to be Newtonian and incompressible with a constant viscosity $\mu$ and density $\rho$. We use a rectilinear coordinate system, $(x, y, z)$, with velocity field $\boldsymbol{u} = (u, v, w)$ in which $x$, $y$ and $z$ denote the streamwise, transverse and vertical coordinates, and $u$, $v$ and $w$ correspond to the components of the velocity field in these directions. The solid substrate and fluid film thickness are located at $z = 0$ and $z = h(x, y, t)$, respectively, and $t$ denotes time.

The spreading process is caused by the initial difference between the surface tension of the surfactant deposition, $\sigma_m$, and the higher surface tension of the underlying uncontaminated film, $\sigma_c$, usually termed the spreading coefficient, $\mathscr{S} = \sigma_c - \sigma_m$. This
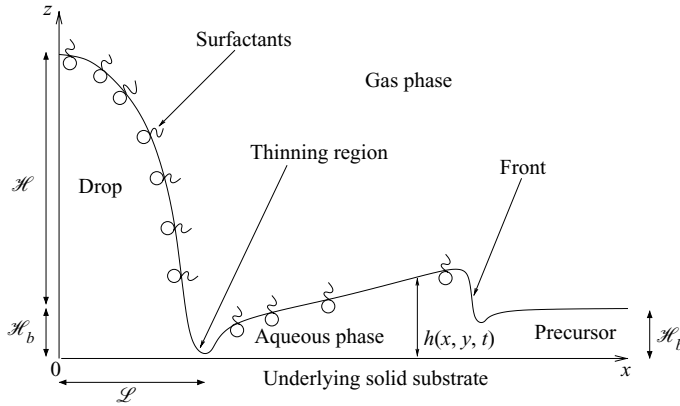
FIGURE 3. Schematic representation of the spreading of deposited surfactant over a thin liquid film.
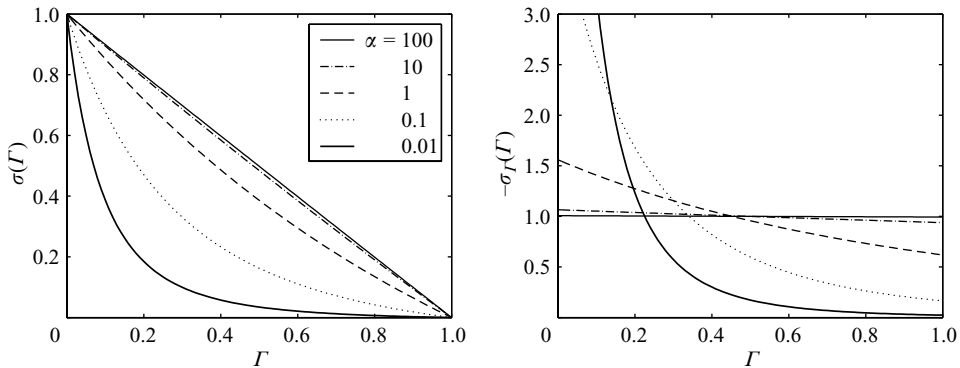


FIGURE 4. Variation of (*a*) $\sigma$ and (*b*) $-\sigma_\Gamma$ with $\Gamma$ for different values of the parameter $\alpha$ according to (2.7).

difference, caused by the contrast in surfactant concentration, drives a Marangoni flow that spreads the deposited surfactant in the direction of the uncontaminated (surfactant-free) surface. In order to describe the dependence of the surface tension, $\sigma$, on the surfactant concentration, $\Gamma$, we choose to adopt an equation of state of the same form as that proposed by Sheludko (1967) and used by Borgas & Grotberg (1988) and Gaver & Grotberg (1990):

$$\frac{\sigma}{\mathscr{S}} = (\alpha + 1)\left(1 - \frac{\Gamma}{\Gamma_m}\left[((\alpha+1)/\alpha)^{1/3} - 1\right]\right)^{-3}, \qquad (2.1)$$

in which $\alpha \equiv \sigma_m/\mathscr{S}$. The assumption that the surfactant is present in dilute concentrations (i.e. large $\alpha$), permits the use of a linearized version of (2.1):

$$\sigma = \sigma_c + (\sigma_\Gamma)_{\Gamma=0}\,\Gamma, \qquad (2.2)$$

where $\sigma_\Gamma = -\mathscr{S}/\Gamma_m$; the subscript $\Gamma$ signifies partial differentiation. Inspection of (2.1) and (2.2) reveals that $\sigma_\Gamma$ is inversely proportional to $\Gamma$ for small $\alpha$ and is approximately constant in the large-$\alpha$ limit (cf. figure 4). Thus, for the nonlinear equation of state the Marangoni stresses are not only dependent on $\Gamma_x$, but also on

$\Gamma$; this is relevant at high concentrations. The effect of $\alpha$ on the fingering instability will be explored later.

In order to derive dimensionless governing equations, we adopt the following scaling:

$$(x, y) = \mathscr{L}(\tilde{x}, \tilde{y}), \quad z = \mathscr{H}\tilde{z}, \quad (u, v) = \mathscr{V}(\tilde{u}, \tilde{v}), \quad w = \epsilon\mathscr{V}\tilde{w}, \quad t = \frac{\mathscr{L}}{\mathscr{V}}\tilde{t}, \quad (2.3)$$

$$p = \frac{\mathscr{L}}{\mathscr{H}}\tilde{p}, \quad \sigma = \mathscr{S}\tilde{\sigma} + \sigma_m, \quad \Gamma = \Gamma_m\tilde{\Gamma}, \tag{2.4}$$

wherein dimensionless quantities are distinguished by the tilde decoration. Here, $\mathscr{V} = \mathscr{S}\mathscr{H}/(\mu\mathscr{L})$ represents a characteristic Marangoni velocity and $\epsilon \equiv \mathscr{H}/\mathscr{L}$ is the drop aspect ratio. The crucial issue to note here is the existence of two vertical length scales (the initial heights of the drop and of the pre-existing thin liquid film): $\mathscr{H}$ and $\mathscr{H}_b$, and we choose to scale $z$ on $\mathscr{H}$. This scaling therefore gives rise to a dimensionless geometrical parameter, $b \equiv \mathscr{H}_b/\mathscr{H}$. Since the spreading of a monolayer of infinitesimally small vertical extent was studied in previous work, only one relevant length scale was present in that direction, namely that of the underlying film thickness. Thus $b \to \infty$ in those studies since $\mathscr{H} \to 0$.

Substitution of the scalings given by equations (2.3) and (2.4) into the equations of conservation of mass and momentum, the normal, shear stress and kinematic boundary conditions at $z = h(x, y, t)$ and the no-slip and no-penetration boundary conditions on $z = 0$, gives rise to the following two-dimensional equations governing the evolution of $h(x, y, t)$ and $\Gamma(x, y, t)$ (after suppression of the tildes) (Jensen & Grotberg 1992; Matar & Troian 1999a, b; Warner et al. 2002b)

$$h_t = -\nabla \cdot \left(\frac{h^2}{2}\nabla\sigma + \mathscr{C}\frac{h^3}{3}\nabla\kappa\right), \tag{2.5}$$

$$\Gamma_t = -\nabla \cdot \left(\Gamma h\nabla\sigma + \mathscr{C}\frac{\Gamma h^2}{2}\nabla\kappa\right) + \frac{1}{Pe}\nabla^2\Gamma, \tag{2.6}$$

where $\kappa = \nabla \cdot \boldsymbol{n}$ is the curvature and the outward pointing normal to the interface, $\boldsymbol{n}$, is $\boldsymbol{n} = \nabla h/|\nabla h|$. In equations (2.5) and (2.6), $\mathscr{C} \equiv \epsilon^2\sigma_m/\mathscr{S}$ represents a capillarity parameter and $Pe \equiv (\mathscr{S}\mathscr{H})/(\mu\mathscr{D})$ is a surface Péclet number reflecting the relative significance of Marangoni-driven to surface diffusive spreading; $\mathscr{D}$ is the surface diffusion coefficient. The equation of state becomes in its rescaled form:

$$\sigma(\Gamma) = \frac{\alpha + 1}{[1 + \Theta(\alpha)\Gamma]^3} - \alpha, \quad \Theta(\alpha) = \left(\frac{\alpha + 1}{\alpha}\right)^{1/3} - 1. \tag{2.7}$$

This function is represented graphically in figure 4 and illustrates the dependence of the surface tension on the parameter $\alpha$. Further, it simplifies in the limit $\alpha \to \infty$ to $\sigma = 1 - \Gamma$; this linear equation of state will often be employed later.

In deriving equations (2.5) and (2.6) we utilize the lubrication approximation by assuming that $\epsilon \ll 1$. Typical experimental parameter values (Afsar-Siddiqui et al. 2003a, b) are $\mathscr{H} \sim 0.1$–$0.01$ cm (estimated from the droplet volume), $\mathscr{L} \sim 1$ cm, $\mathscr{H}_b \sim 10^{-3}$–$10^{-2}$ cm, $\mu \sim 1$ cP, $\mathscr{D} \sim 10^{-5}$ cm$^2$ s$^{-1}$, $\mathscr{S} \sim 40$ dyn cm$^{-1}$, $\sigma_m \sim 40$ dyn cm$^{-1}$, which lead to the following range of dimensionless parameters:

$$\epsilon \sim 0.1\text{--}0.01, \quad b \sim 0.1\text{--}0.01, \quad \mathscr{C} \sim 10^{-4}\text{--}10^{-2}, \quad Pe \sim 10^6\text{--}10^7. \tag{2.8}$$

Inspection of these ranges suggests that the use of lubrication theory is permissible and that the flow is primarily driven by Marangoni stresses with surface diffusion and

capillarity providing suitable physical regularization. Next, we present the equations governing the dynamics of the flow in the absence of perturbations, the base state, and that of the applied linear disturbances.

### 2.2. *Base state and disturbance equations*

The stability of the streamwise spreading process to initially infinitesimal transverse disturbances is investigated by inserting the following decomposition into equations (2.5) and (2.6):

$$(h, \Gamma)(x, y, t) = (h_0, \Gamma_0)(x, t) + (h_1, \Gamma_1)(x, t)e^{iky},$$

where $k$ denotes the disturbance wavenumber and the subscripts 0 and 1 signify base state and disturbance quantities. Linearization of equations (2.5) and (2.6) and separation of the resultant equations into those governing the dynamics of the one-dimensional base state and those describing the evolution of the disturbances yields

$$h_{0t} = -\frac{1}{2}\left(h_0^2\sigma_{0x}\right)_x - \frac{\mathscr{C}}{3}\left(h_0^3\kappa_{0x}\right)_x, \tag{2.9}$$

$$\Gamma_{0t} = -(\Gamma_0 h_0 \sigma_{0x})_x - \frac{\mathscr{C}}{2}\left(\Gamma_0 h_0^2\kappa_{0x}\right)_x + \frac{1}{Pe}\Gamma_{0xx}, \tag{2.10}$$

for the base state and

$$h_{1t} = -\frac{1}{2}\left[\left(h_0^2\sigma_{1x} + 2h_0 h_1\sigma_{0x}\right)_x - k^2 h_0^2\sigma_1\right] - \frac{\mathscr{C}}{3}\left[\left(h_0^3\kappa_{1x} + 3h_0^2\kappa_{0x}h_1\right)_x - k^2 h_0^3\kappa_1\right], \tag{2.11}$$

$$\Gamma_{1t} = -\left[(h_0\Gamma_0\sigma_{1x} + h_1\Gamma_0\sigma_{0x} + h_0\Gamma_1\sigma_{0x})_x - k^2\Gamma_0 h_0\sigma_1\right] + \frac{1}{Pe}(\Gamma_{1xx} - k^2\Gamma_1)$$

$$- \frac{\mathscr{C}}{2}\left[\left(\Gamma_0 h_0^2\kappa_{1x} + 2h_0\Gamma_0\kappa_{0x}h_1 + h_0^2\kappa_{0x}\Gamma_1\right)_x - k^2\Gamma_0 h_0^2\kappa_1\right], \tag{2.12}$$

for the applied disturbances, and in which $\sigma_0 = (\alpha + 1)[1 + \Theta(\alpha)\Gamma_0]^{-3} - \alpha$, and $\sigma_1 = -3(\alpha + 1)\Theta(\alpha)\Gamma_1[1 + \Theta(\alpha)\Gamma_0]^{-4}$. In equations (2.11) and (2.12), $\kappa_0 = h_{0xx}$ and $\kappa_1 = h_{1xx} - k^2 h_1$. An often used ad-hoc addition to thin-layer models is the retention of the full curvature (Ruschak 1978; Braun *et al.* 1999; Matar & Craster 2001), to provide a regularizing effect in the region where the thin underlying film meets the steep surfac-tant deposition. In this work, however, we have simply used the leading-order curva-ture, $\kappa = \nabla^2 h$, and checked that use of the full curvature, $\kappa_0 = h_{0xx}/(1 + \epsilon^2 h_{0x}^2)^{3/2}$ and $\kappa_1 = (h_{1xx} - k^2 h_1)/(1 + \epsilon^2 h_{0x}^2)^{3/2}$, leads to only minor quantitative differences. Therefore, we have not utilized the full curvature in the numerical results shown herein.

### 2.3. *Growth measures*

The spatially and temporally evolving base state, $h_0$ and $\Gamma_0$, that satisfies equations (2.9) and (2.10), precludes a normal-mode eigenvalue analysis. To circumvent this potential complication, two approaches are followed: we conduct a transient growth analysis (TGA) of the evolving base state and a linear stability analysis in the quasi-steady-state approximation (QSSA). The first approach follows previous investigators (Shen 1961; Matar & Troian 1998, 1999*a*,*b*; Warner *et al.* 2002*b*) who employ the concept of 'momentary stability' as a measure of the instantaneous stability of a time-dependent base flow at time $t = \tau$. We begin by defining the 'energy' of a disturbance or a base state quantity, $E_q$, as

$$E_q(\tau) \equiv \int_0^\infty (q - q_\infty)^2(x, \tau)\,\mathrm{d}x, \tag{2.13}$$

in which $q = (h_0,\ \Gamma_0,\ h_1,\ \Gamma_1)$ and $q_\infty = (b,\ 0,\ 0,\ 0)$. Note that these are not physical energies, but simply provide a convenient measure of growth. We then define an amplification ratio of the 'energy' of both the height and concentration disturbances at time $t = \tau$ to that at $t = 0$ as $G_h$ and $G_\Gamma$, respectively,

$$G_h(t = \tau) \equiv \frac{\left(E_{h_1}/E_{h_0}\right)(t = \tau)}{\left(E_{h_1}/E_{h_0}\right)(t = 0)}, \qquad (2.14)$$

$$G_\Gamma(t = \tau) \equiv \frac{\left(E_{\Gamma_1}/E_{\Gamma_0}\right)(t = \tau)}{\left(E_{\Gamma_1}/E_{\Gamma_0}\right)(t = 0)}. \qquad (2.15)$$

The overall instantaneous growth rate of a disturbance to the film thickness or surfactant concentration, $\lambda_h$ and $\lambda_\Gamma$, is then given by

$$\left.\begin{aligned}
\lambda_h(t = \tau) &= \frac{1}{G_h}\frac{\mathrm{d}G_h}{\mathrm{d}t} = \lambda_{h_1} - \lambda_{h_0}, \\
\lambda_\Gamma(t = \tau) &= \frac{1}{G_\Gamma}\frac{\mathrm{d}G_\Gamma}{\mathrm{d}t} = \lambda_{\Gamma_1} - \lambda_{\Gamma_0},
\end{aligned}\right\} \qquad (2.16)$$

in which $\lambda_{h_0}$, $\lambda_{h_1}$, $\lambda_{\Gamma_0}$ and $\lambda_{\Gamma_1}$ are given by

$$\lambda_{h_0} = \frac{1}{2E_{h_0}}\frac{\mathrm{d}E_{h_0}}{\mathrm{d}t}, \qquad \lambda_{\Gamma_0} = \frac{1}{2E_{\Gamma_0}}\frac{\mathrm{d}E_{\Gamma_0}}{\mathrm{d}t}, \qquad (2.17)$$

$$\lambda_{h_1} = \frac{1}{2E_{h_1}}\frac{\mathrm{d}E_{h_1}}{\mathrm{d}t}, \qquad \lambda_{\Gamma_1} = \frac{1}{2E_{\Gamma_1}}\frac{\mathrm{d}E_{\Gamma_1}}{\mathrm{d}t}. \qquad (2.18)$$

Thus the overall growth rate is defined as the difference between the normalized growth rate of the disturbances and those of the base state. Note that in the case of temporally varying base states, it is still possible to have instability despite a negative disturbance growth rate provided the base state growth rate is even more negative (Drazin & Reid 1982). Note further that (2.16) reduces to a constant growth rate, $\lambda$, say, for a disturbance to a steady base state of the form $\exp(\lambda t)\exp(iky)$.

The second approach, conducted in the QSSA, assumes that the rate of change with respect to time of the perturbations far exceeds that of the base state. For given values of $b$, $\mathscr{C}$ and $Pe$, the base state is then 'frozen' at a chosen time, $t_\mathrm{f}$, and the linear stability characteristics of this state are then determined via solution of equations (2.11) and (2.12) for a prescribed value of $k$ as an initial value problem for long times. The quasi-static growth rates, $\lambda_\mathrm{qssa}$, associated with $t_\mathrm{f}$ and $k$ are then extracted and a 'dispersion curve' constructed. The results from the TGA and QSSA analyses are presented next.

# 3. Results

In this section, we present the results of our numerical computations. Base state profiles are presented first followed by the stability characteristics of the evolving base state and those obtained in the QSSA. These, in turn, are followed by a breakdown of the disturbance growth rate and the results of the direct numerical simulations. We begin, however, by providing details of the numerical procedures used to carry out the computations.

## 3.1. *Numerical procedure*

The highly efficient PDE solver, EPDCOL (Keast & Muir 1991; Sincovec & Madsen 1979) which is a numerical scheme designed for the solution of highly nonlinear

parabolic equations, based on the method of lines using finite-element collocation in space and Gear's method in time, is used to carry out the one-dimensional computations. This provided accurate and well-resolved solutions of the base state and disturbance equations, (2.9)–(2.12), that feature shock-like solutions at the surfactant leading edge and severe and rapid thinning near the origin (Jensen & Grotberg 1992; Craster & Matar 2000). In two-dimensional computations, an alternating direction implicit (ADI) scheme was developed and it is described in the Appendix. Both codes were cross-verified, when appropriate, against each other and with existing solutions.

EPDCOL has previously been used to obtain efficient and accurate solutions of thin-film equations in related problems (Craster & Matar 2000; Matar *et al.* 2002; Warner *et al.* 2002*a, b*). The maximum mesh spacing used is 0.01 in the one-dimensional computations; convergence is achieved upon refinement of the spatial mesh.

One-dimensional solutions for the evolving base state are obtained starting from the following initial conditions:

$$h(x, 0) = (1 + b - x^2)H(1 - x) + bH(x - 1), \quad \Gamma(x, 0) = H(1 - x), \quad (3.1)$$

where $H(x) = \frac{1}{2}[1 + \tanh(Kx)]$; $K = 100$ in all one-dimensional computations, for two-dimensional computations we use $K = 20$. These initial conditions mimic the deposition of a cap of fluid covered by surfactant of essentially uniform concentration on an undisturbed film of much smaller thickness. The initial conditions for $h_1$ and $\Gamma_1$ represent disturbances that are localized near the flow origin, away from the point of contact between the surfactant deposition and the underlying thin film:

$$h_1(x, 0) = \Gamma_1(x, 0) = \exp(-x^2); \quad (3.2)$$

other choices of initial conditions give rise to quantitative rather than qualitative differences.

The numerical solutions are obtained subject to the following boundary conditions:

$$\left. \begin{array}{llll} h_{0x}(0, t) = h_{0xxx}(0, t) = 0, & h_0(L_x, t) = b, & h_{0x}(L_x, t) = 0, \\ h_{1x}(0, t) = h_{1xxx}(0, t) = 0, & h_1(L_x, t) = 0, & h_{1x}(L_x, t) = 0, \end{array} \right\} \quad (3.3)$$

$$\left. \begin{array}{ll} \Gamma_{0x}(0, t) = 0, & \Gamma_0(L_x, t) = 0, \\ \Gamma_{1x}(0, t) = 0, & \Gamma_1(L_x, t) = 0, \end{array} \right\} \quad (3.4)$$

where $L_x$ is the length of the computational domain in the $x$-direction; equations (3.3) and (3.4) correspond to symmetry conditions at the flow origin and decay far downstream; changing the conditions for the disturbances at $L_x$ to $h_{1xxx} = h_{1x} = \Gamma_{1x} = 0$ makes no difference to the results.

In obtaining numerical solutions, the length of the computational domain in the $x$-direction, $L_x$, is chosen to be sufficiently large that the solutions obtained are independent of $L_x$. In the one-dimensional computations $L_x \leqslant 30$. Finally, solutions are generated for $0 \leqslant t \leqslant 10^5$, $0.01 \leqslant b \leqslant 1$, $10^{-4} \leqslant \mathscr{C} \leqslant 10^{-2}$, $0.01 \leqslant \alpha < \infty$ and $10^2 \leqslant Pe \leqslant 10^5$. The base state profiles are presented next.

### 3.2. Base state

Prior to presenting the results of the stability analyses, we briefly examine the evolution of the base state profiles. Figure 5 depicts numerical solutions of equations (2.9) and (2.10) using the linear equation of state ($\alpha \rightarrow \infty$) for $b = 0.01$, $\mathscr{C} = 10^{-3}$ and $Pe = 10^5$, which corresponds to the case of a surfactant deposition spreading over a precursor-like thin liquid film driven predominantly by Marangoni stresses in the presence of weak surface diffusion and capillarity. The initially steep gradients of
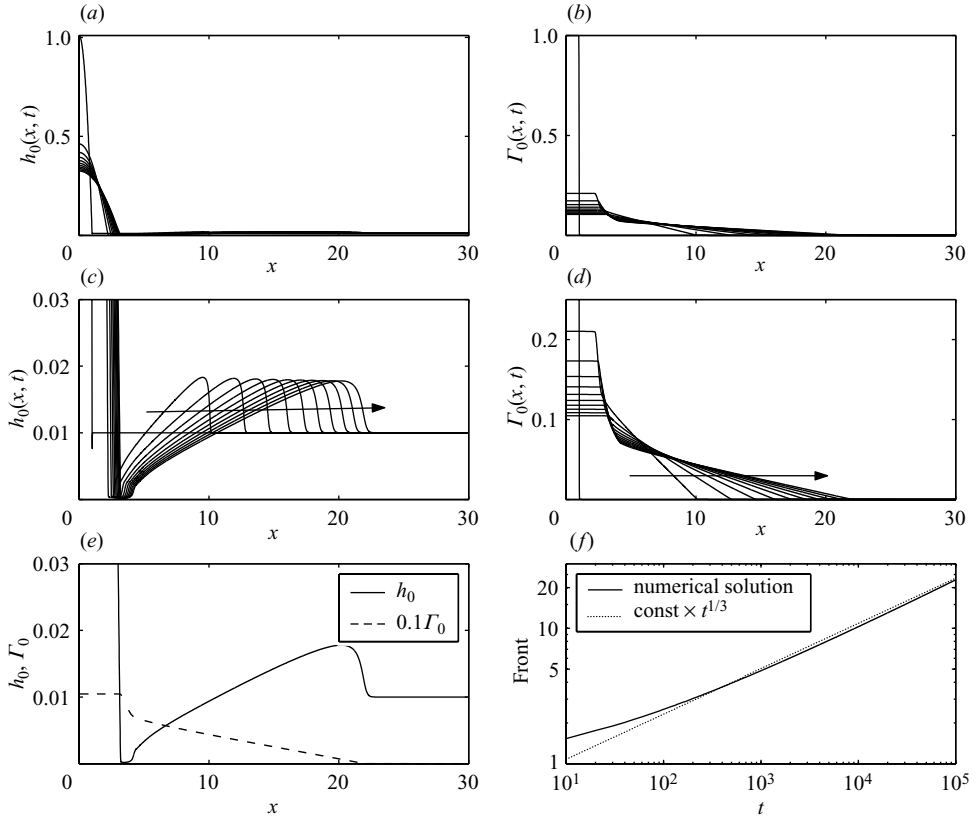
FIGURE 5. Base state profiles generated with the linear equation of state ($\alpha \to \infty$), parameters $b = 0.01$, $\mathscr{C} = 10^{-3}$, $Pe = 10^5$ and $t = 0$ to $10^5$ in ten equal time intervals. (*a*, *b*) $h_0$ and $\Gamma_0$ over the entire computational domain, with enlarged versions of these profiles in (*c*) and (*d*), respectively; (*e*) a superposition of $h_0$ and $0.1 \times \Gamma_0$ at $t = 10^5$ and (*f*) the temporal variation of the frontal position, that is, the spatial location of the maximal value of $h_0$ at the leading front, together with the theoretical power-law dependence for the case of rectilinear spreading of a finite amount of surfactant on a thin film (Jensen & Grotberg 1992). The arrows in (*c*) and (*d*) and subsequent figures indicate the direction of increasing time.

surfactant concentration present in the surfactant deposition, shown in figure 5(*b*), give rise to surface tension gradients and Marangoni stresses. These drive spreading towards the uncontaminated regions of the underlying thin liquid film, which leads to the subsequent relaxation of these gradients and of the driving force for the spreading. This Marangoni-driven spreading induces large deformations in this liquid film, leading to the formation of a thickened front of thickness almost twice its undisturbed value, and severe thinning upstream where the thin film meets the surfactant deposition, as shown in figures 5(*a*) and 5(*c*).

The concentration profile, on the other hand, exhibits three distinct regions: a region of uniform concentration in the deposition, a region of approximately constant but steep gradient in the thinning region, which adjusts rapidly onto a third region of constant but shallow gradient, coinciding with the region of constant gradient in the film thickness (see figures 5*d* and 5*e*). Due to the large viscous retardation experienced in the thin region, most of the surfactant deposition remains as a cap spreading slowly over a much thinner liquid film. This is evident even at $t = 10^5$,

corresponding to approximately $10^3$ dimensional units; this is in agreement with experimental observations (Afsar-Siddiqui *et al.* 2003*a*, *b*) and is shown in figures 5(*a*) and 5(*c*). In contrast, the front travels more rapidly with a power-law dependence on time, which agrees with theoretical predictions for the rectilinear spreading of a finite amount of surfactant (Jensen & Grotberg 1992), as shown in figure 5(*f*).

Next, we examine the effect of varying $b$, $\mathscr{C}$, $\alpha$ and $Pe$ on the structure of the base state profiles. Inspection of figures 6(*a*) and 6(*b*) reveals that increasing the value of $b$ leads to more rapid surfactant spreading, due to a concomitant decrease in viscous retardation, and milder deformations manifested by less severe thinning and broader thinning regions and fronts in $h_0$; the slopes in $\Gamma_0$ also become less steep with increasing $b$. Decreasing the value of $\mathscr{C}$ appears to have a similar effect: the relative significance of capillarity is decreased leading to more severe film deformations, as shown in figures 6(*c*) and 6(*d*). Increasing the magnitude of $Pe$, that is, decreasing the relative significance of surface diffusion, also has a similar effect leading to sharp variations in $\Gamma_0$. The effect of the parameter, $\alpha$, which controls the degree of nonlinearity in the equation of state, is shown in figures 6(*g*) and 6(*h*); smaller values of $\alpha$ cause a substantial widening and an associated more severe degree of thinning of the region between the drop and the front. In addition the rate of propagation of the front is increased. The dependence of the base flow on these parameters will be used to interpret the stability results, which are presented next.

### 3.3. *Linear stability*

#### 3.3.1. *Evolving base state*

We commence the presentation of the stability results by examining the stability of an evolving base state to transverse disturbances. Figure 7 shows the temporal variation of the amplification ratio of applied height and concentration perturbations, $G_h(t)$ and $G_\Gamma(t)$, together with the instantaneous growth rates, $\lambda_h$ and $\lambda_\Gamma$, for $b = 0.1$, $\mathscr{C} = 10^{-3}$, $Pe = 10^5$, $\alpha \to \infty$ (that is, a linear equation of state), and $0 \leqslant k \leqslant 70$. It is clearly seen that both $G_h$ and $G_\Gamma$ increase by several orders of magnitude, indicating the presence of a flow instability, which is also evident upon inspection of the temporal variation of $\lambda_h$ and $\lambda_\Gamma$. Moreover, following an initial short time period (approximately equal to ten dimensionless time units) during which the $k = 0$ disturbance is dominant (see inset of figure 7), a transverse disturbance of intermediate wavenumber ($k = 20$ in this case) appears to be maximally amplified; this indicates the existence of a selected wavelength for the ensuing pattern formation. Large-wavenumber disturbances, however, appear to decay under the action of the stabilizing capillary forces.

To examine the structure of the growing perturbations, in figure 8 we plot numerical solutions of $h_0$ and $\Gamma_0$, together with $h_1$ and $\Gamma_1$ associated with the maximally amplified 'mode' although, interestingly, the magnitude of $h_1$ far exceeds that of $\Gamma_1$. Inspection of figures 8(*a*) and 8(*b*) reveals that $h_1$ and $\Gamma_1$ exhibit large peaks in the vicinity of the trough in $h_0$ and are approximately zero-valued elsewhere. In contrast to the results presented in previous work, Matar & Troian (1998, 1999*a*, *b*), the disturbances appear to be 'pinned' in the thinning region rather than at the thickened front. Furthermore, this occurs despite the absence of intermolecular interactions such as van der Waals forces. The results shown in figure 8 appear to agree with previous experimental studies (Troian *et al.* 1989; Afsar-Siddiqui *et al.* 2003*a*, *b*) in which fingering was observed to occur in the thinning region behind the advancing front. It is also worthy of mention, however, that the structure of the $k = 0$ mode, which is dominant at early times, is quite different from that of the $k > 0$ modes: in addition to targeting the
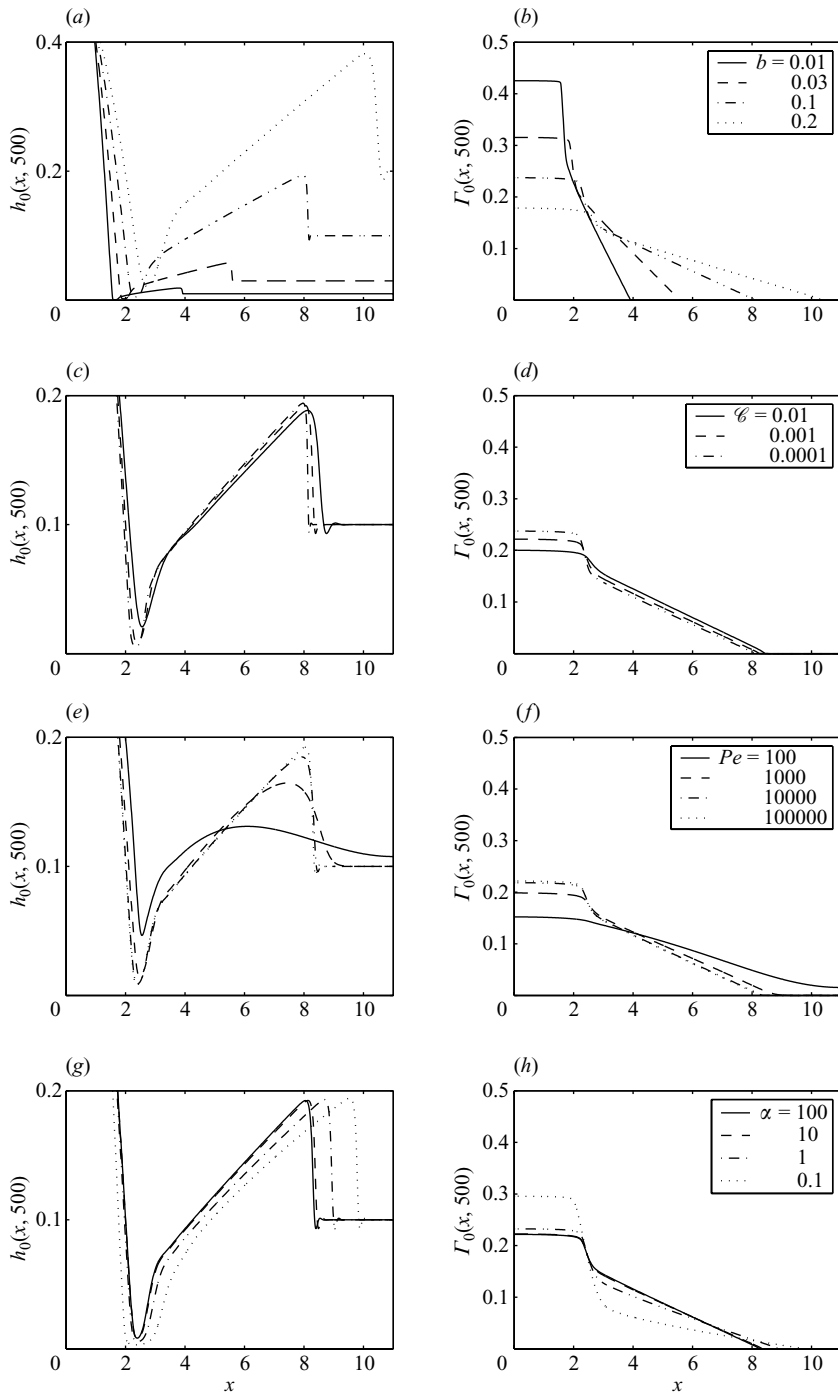
FIGURE 6. Dependence of the base state profiles on system parameters. $(a, b)$ Effect of $b$; $(c, d)$ effect of $\mathscr{C}$; $(e, f)$ effect of $Pe$; $(g, h)$ effect of $\alpha$. Unless otherwise stated in the legends the parameter values are $b = 0.1$, $\mathscr{C} = 10^{-3}$, $Pe = 10^5$, $\alpha \to \infty$ and $t = 500$.
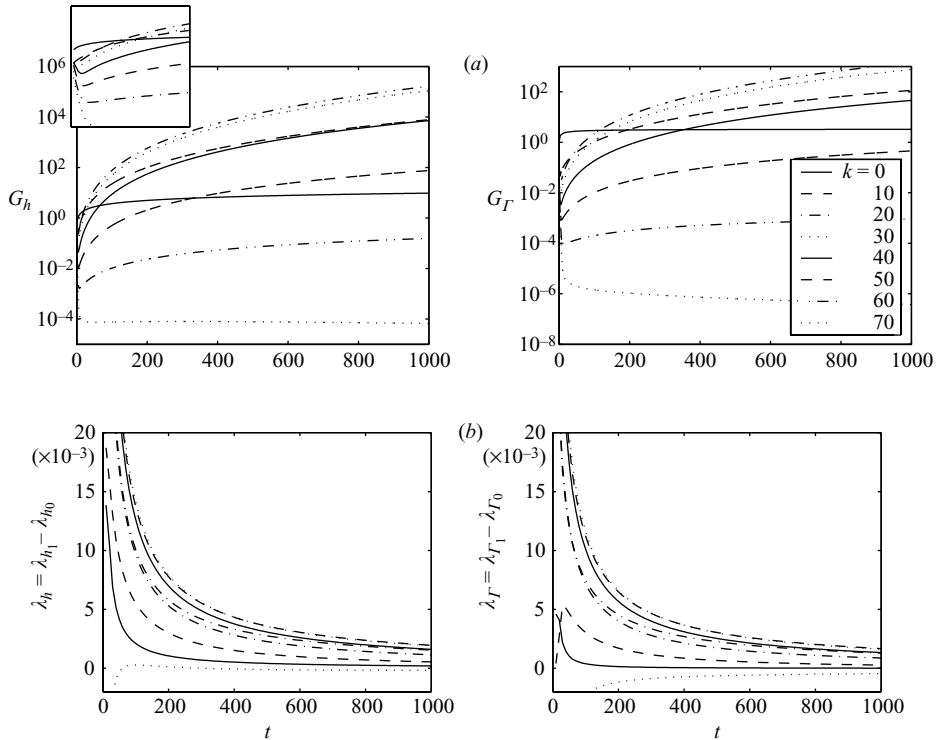
FIGURE 7. Transient growth analysis of the evolving base state: temporal variation of (*a*) the amplification ratios and (*b*) growth rates of applied disturbances with the wavenumber, $k$, varying parametrically. The inset for $G_h$ is for $0 < t < 50$, $10^{-4} < G_h < 10^2$ and highlights the small-time behaviour of the various wavenumbers. The parameter values are $b = 0.1$, $\mathscr{C} = 10^{-3}$ and $Pe = 10^5$ with a linear equation of state $\alpha \to \infty$.

thinning region, this mode appears to target the advancing front as well, as shown in figure 9; this mode is overtaken by $k > 0$ modes at a relatively early stage of the spreading process.

Qualitatively similar results to those shown in figure 8 were also observed with $b = 0.01$ and all other parameters held constant. In this case, the 'selected mode' is associated with a much larger wavenumber ($k = 150$ compared to $k = 20$ in figure 8) that once again appears to target the trough in $h_0$; this is shown in figures 10 and 11. Also evident from figure 10 is the explosive growth exhibited by $G_h(t)$, which increases by more than 10 orders of magnitude over 200 dimensionless time units. These results indicate that decreasing $b$ has a destabilizing effect on the spreading process, characterized by a more rapid growth and a shift in the selected mode towards larger $k$.

Next we study the effect of system parameters on its stability by examining the dependence of $G_h(t)$ and $G_\Gamma(t)$ on $b$, $\mathscr{C}$, $\alpha$, and $Pe$ for a disturbance of $k = 10$; this dependence is shown in figure 12. The effect of varying $b$, shown in figure 12(*a*) confirms the conclusions drawn based on the results shown in figures 7–11: decreasing $b$, which helps promote pinning and subsequent growth of disturbances in the thinning region, is strongly destabilizing with $b > 0.5$ rendering the system stable at $\mathscr{C} = 10^{-3}$, $\alpha \to \infty$ and $Pe = 10^5$. It is instructive at this stage to also compare to the case of a surfactant monolayer spreading on a thin film (not shown) previously studied in the
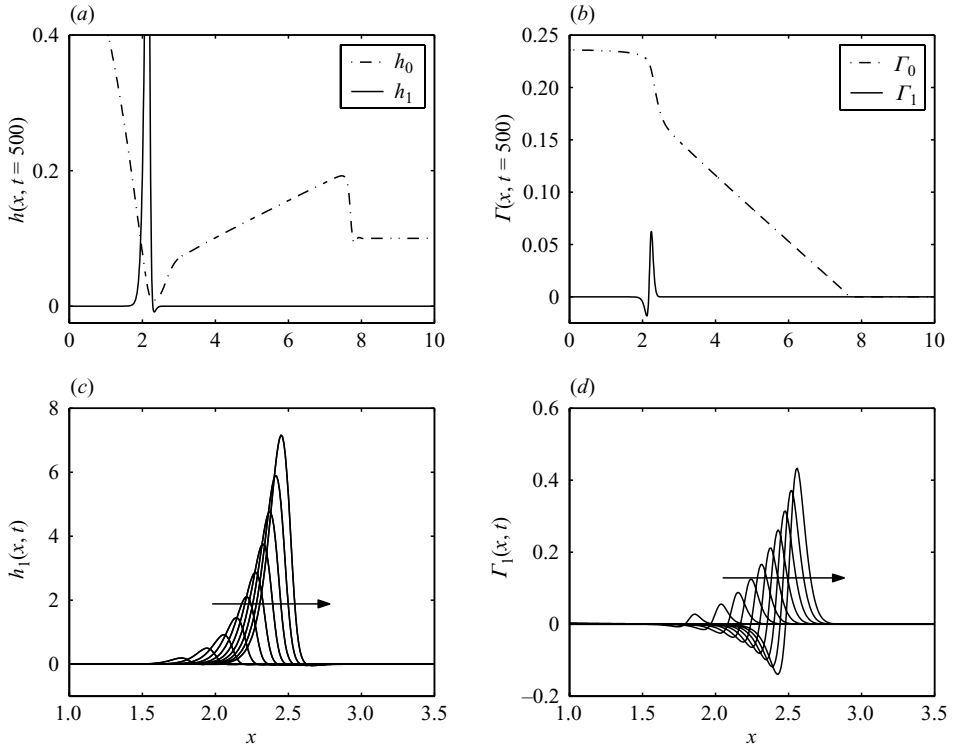
FIGURE 8. Transient growth analysis of an evolving base state: spatial structure of the base state and disturbances. Numerical solutions of the base state, $h_0$ and $\Gamma_0$, are shown superimposed together with the disturbance variables, $h_1$ and $\Gamma_1$, in ($a$) and ($b$), and in which the linear disturbances are scaled by a factor of 0.005. ($c$) and ($d$) The temporal development of the disturbances, at time intervals of $t = 100$ from $t = 0$ up to $t = 1000$, with the arrows showing the direction of increasing time. The parameter values are as in figure 7, and $k = 20$.
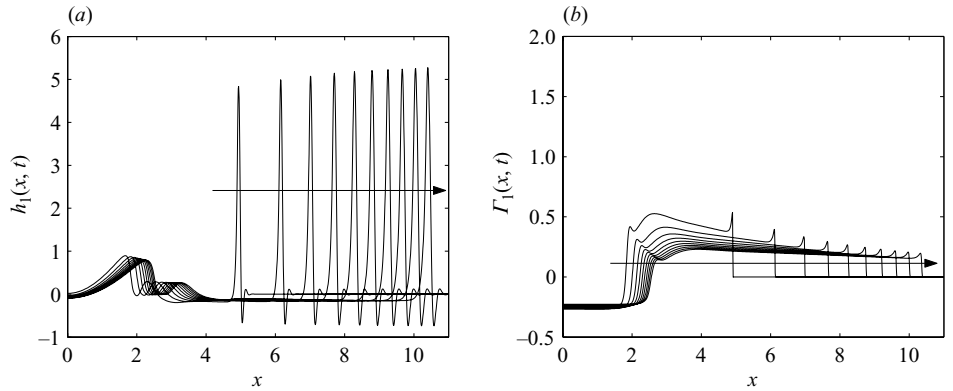


FIGURE 9. Evolution of the $k = 0$ disturbance for $t = 0$ to $t = 1000$ with ten equal time steps and the same parameter values as in figure 8.

literature (Matar & Troian 1997, 1998, 1999$a$, $b$) and is known to also exhibit decay. These results indicate that the presence of a sufficiently large difference in elevation between the surfactant deposition and the underlying thin film (that is, small $b$ values) for a given set of parameters appears to be a necessary condition for instability.
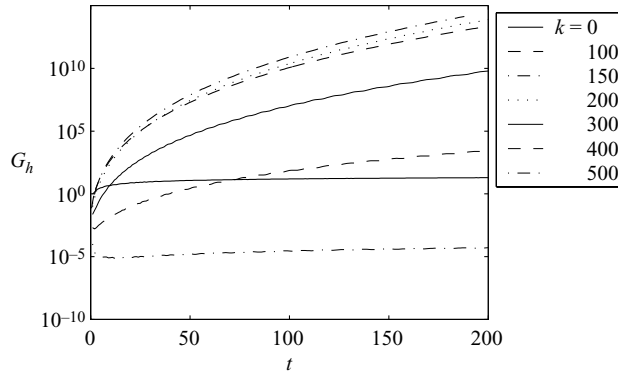
FIGURE 10. Temporal variation of the amplification ratio of disturbances to the film thickness, $G_h$, of wavenumber $k$ to an evolving base state; the parameter values are as in figure 7 except that $b = 0.01$.
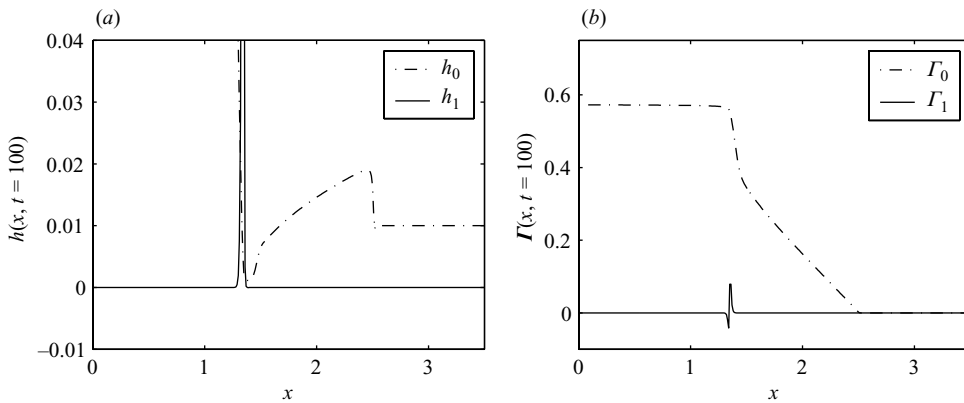


FIGURE 11. Spatial structure of $h_0$ and $\Gamma_0$, together with $h_1$ and $\Gamma_1$, with a scaling factor of $10^{-7}$ multiplying the disturbance variables $h_1$ and $\Gamma_1$, at $t = 100$ and for the same parameter values as in figure 10, and $k = 150$.

Figures 12($c$) and 12($d$) show the effect of varying $\mathscr{C}$ on $G_h(t)$ and $G_\Gamma(t)$ with $b = 0.1$, $\alpha \to \infty$ and $Pe = 10^5$. Increasing $\mathscr{C}$, which reflects an increase in the relative magnitude of capillarity, exerts a stabilizing effect. This is due to the associated smoothing of the $h_0$ and $\Gamma_0$ profiles and the relative decrease in thickness contrast in the thinning region at a given time, as shown in figure 6($c$); this makes it less likely for disturbances to be pinned and to undergo growth in the thinning region. This stabilizing effect, however, saturates with decreasing $\mathscr{C}$: the curves associated with $\mathscr{C} = 10^{-3}$ and $\mathscr{C} = 10^{-4}$ in figures 12($a$) and ($d$) are virtually indistinguishable.

The effect of varying $Pe$ on $G_h(t)$ and $G_\Gamma(t)$ is shown in figures 12($e$) and 12($f$) with $b = 0.1$, $\mathscr{C} = 10^{-3}$ and $\alpha \to \infty$. Increasing $Pe$, which reflects an increase in the relative dominance of Marangoni stresses, promotes disturbance growth, although this effect also appears to saturate: the curves associated with $Pe = 10^4$ and $Pe = 10^5$ are almost indistinguishable. Decreasing $Pe$ to a value of 100, that is promoting surface diffusion relative to Marangoni effects, promotes stability. These results are explained by examining figure 6($e$), which shows that decreasing values of $Pe$ lead to milder deformations and shallower troughs; also evident is the insensitivity of $h_0$ and $\Gamma_0$ to changes in $Pe$ beyond $Pe \approx 10^4$.
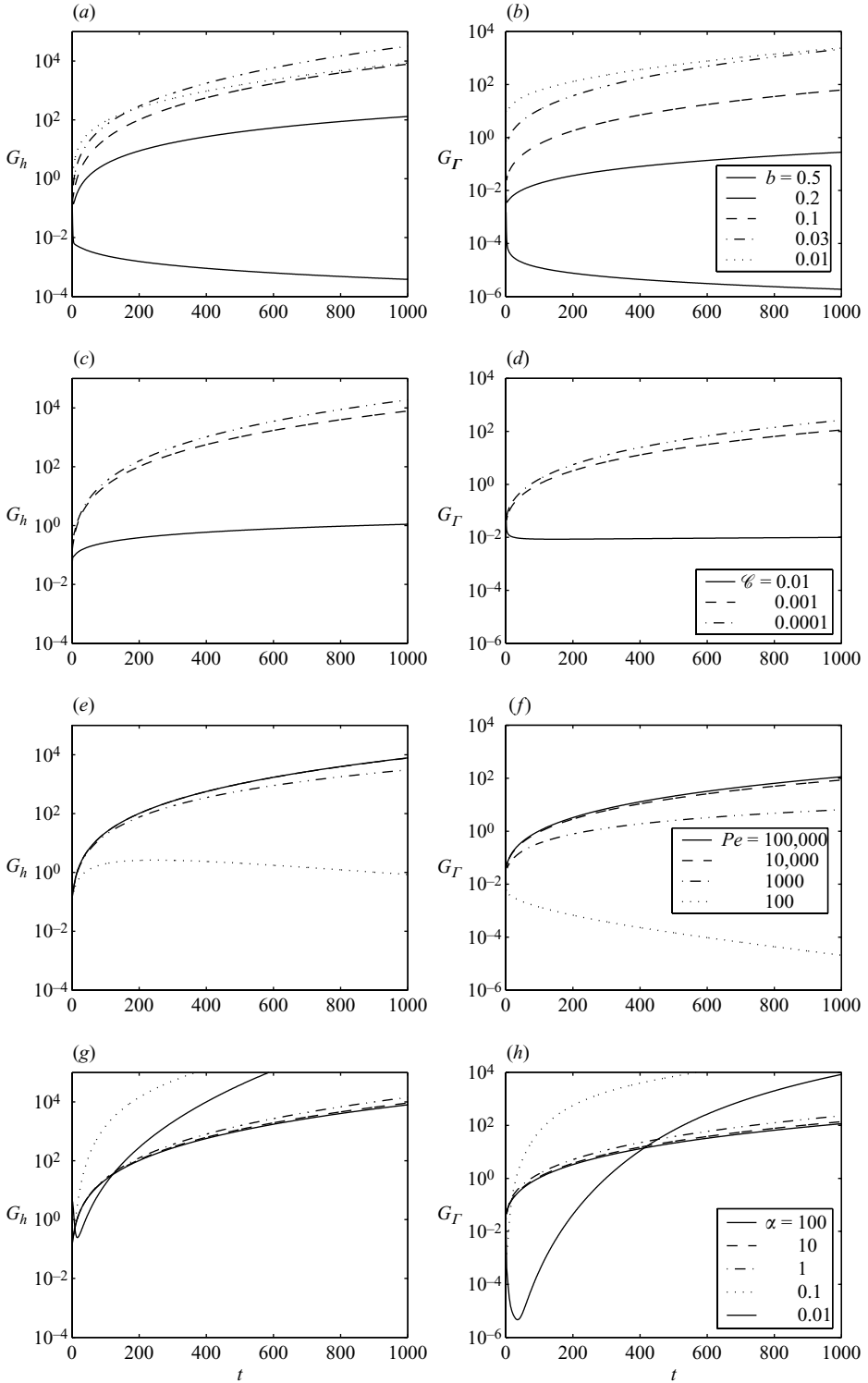
FIGURE 12. Effect of varying $b$, $\mathscr{C}$, $Pe$ and $\alpha$ on the amplification ratios, $G_h$ and $G_\Gamma$, of a disturbance of $k = 10$ to an evolving base state, shown in $(a,b)$, $(c,d)$, $(e,f)$ and $(g,h)$, respectively. Unless otherwise stated in the legend the parameter values are $b = 0.1$, $\mathscr{C} = 10^{-3}$, $\alpha \to \infty$ and $Pe = 10^5$.
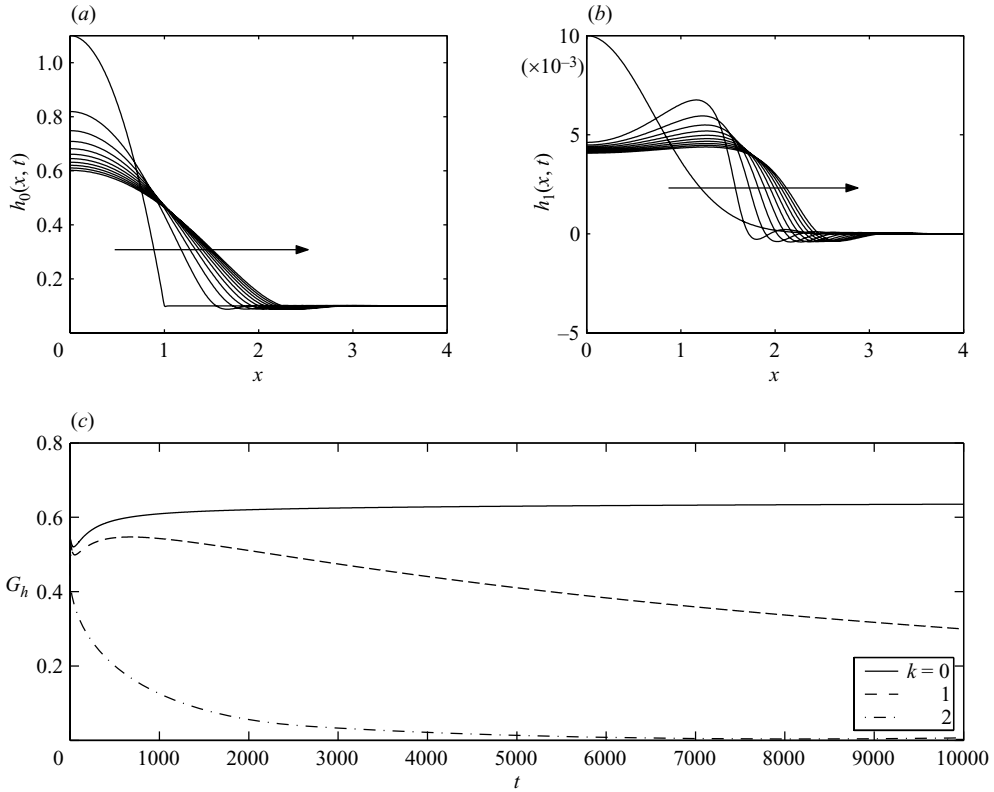
FIGURE 13. Transient growth analysis of an evolving base state in the absence of surfactant. Numerical solutions of $h_0$ and $h_1$ are shown in (a) and (b), respectively, for $t = 0$ to $t = 10^4$ in ten equal time steps, while the temporal variation of the amplification ratio of thickness disturbances is shown in (c) for various $k$ values. The parameter values are $b = 0.1$ and $\mathscr{C} = 10^{-3}$.

The effect of varying $\alpha$ on $G_h(t)$ and $G_\Gamma(t)$ is shown in figures 12(g) and 12(h) with $b = 0.1$, $\mathscr{C} = 10^{-3}$ and $Pe = 10^5$. Larger values of $\alpha$, which correspond to the equation of state in the linear regime when surfactants are present only in dilute concentrations, results in instabilities exhibiting growth of relatively low magnitude; there appears to be little difference in growth rates for values $\alpha \geqslant 10$, in each case attaining growth rates almost indistinguishable from those associated with the linear approximation, $\sigma = 1 - \Gamma$. Decreasing $\alpha$ below this value results in substantial promotion of instability; however, very small values may exhibit decay, or only very weak growth at early times. Thus there appears to be some intermediate value of $\alpha$ in the range $0 < \alpha < 1$ which maximizes initial growth. Note, however, that the nonlinear equation of state is not necessary for instability, and for simplicity and clarity, we only utilize the linear equation of state henceforth.

The results presented so far appear to indicate that unstable flow is promoted by a decrease in $b$, $\mathscr{C}$ and $\alpha$ and an increase in $Pe$. We have also sought to separate the effects of Marangoni stresses from those associated with adverse mobility, which are related to large thickness contrasts between the surfactant deposition and underlying film thickness. To this end, we have examined the stability of an uncontaminated mound of liquid relaxing over a thin film with $b = 0.1$ and $\mathscr{C} = 10^{-3}$. Note that in this case $\mathscr{C} = \epsilon^2$ since $\sigma_c = \sigma_m$ due to the absence of surfactant. Inspection of figure 13
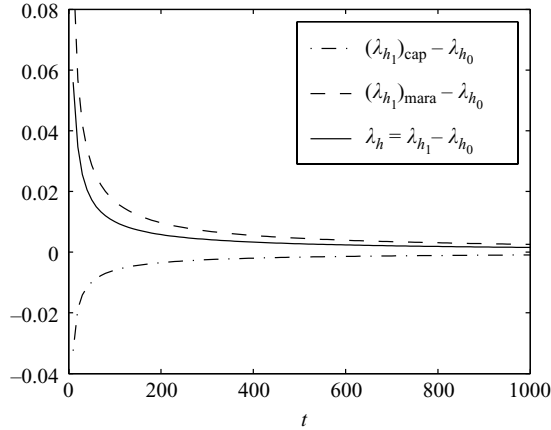
FIGURE 14. Decomposition of the overall instantaneous growth rate, $\lambda_h(t)$, of a film thickness disturbance of $k = 10$ to an evolving base state with $b = 0.1$, $\mathscr{C} = 10^{-3}$ and $Pe = 10^5$ (a linear equation of state is utilized from hereon in all figures).

shows that this case is stable; we have checked that this is also true for larger values of $k$ and the same parameters as those in figure 13 as well as for smaller $b$ values. This then indicates that the presence of Marangoni stresses appears to be necessary for instability.

### 3.3.2. *Energy decomposition*

To isolate the destabilizing mechanism, the instantaneous growth rate of the disturbances, $\lambda_q$ ($q = h_1, \Gamma_1$), is decomposed into its constituent components. We examine only $\lambda_{h_1}$ (examination of $\lambda_{\Gamma_1}$ leads to the same conclusions) and decompose it into two parts:

$$\left(\lambda_{h_1}\right)_{\text{mara}} = \left(\int_0^\infty \frac{1}{2}\left[\left(h_0^2\Gamma_{1x} + 2h_0h_1\Gamma_{0x}\right)_x - k^2h_0^2\Gamma_1\right]h_1\,\mathrm{d}x\right)\Big/ E_{h_1}, \qquad (3.5)$$

$$\left(\lambda_{h_1}\right)_{\text{cap}} = \left(\int_0^\infty -\frac{\mathscr{C}}{3}\left[\left(h_0^3\kappa_{1x} + 3h_0^2h_1\kappa_{0x}\right)_x - k^2h_0^3\kappa_1\right]h_1\,\mathrm{d}x\right)\Big/ E_{h_1}. \qquad (3.6)$$

Equations (3.5) and (3.6) correspond to the growth rate associated with Marangoni stresses and capillarity, respectively: positive (negative) values of these quantities imply that their associated physical mechanisms are destabilizing (stabilizing). A similar approach was followed by Spaid & Homsy (1996) and Kataoka & Troian (1997) in their work on fingering instabilities in gravitationally and thermally driven dynamic contact lines, respectively, as well as by Matar & Troian (1999b) in their study of a reduced version of the present problem.

Figure 14 shows the temporal variation of $(\lambda_{h_1})_{\text{mara}}$ and $(\lambda_{h_1})_{\text{cap}}$ with $k = 10$, $b = 0.1$, $\mathscr{C} = 10^{-3}$, $\alpha \to \infty$, and $Pe = 10^5$. Inspection of this plot reveals that, following an initial period characterized by relatively large instantaneous growth rates, $\lambda_h$ decreases to an approximately constant value at long times. Throughout the period of dimensionless times examined, $(\lambda_{h_1})_{\text{mara}} > 0$, while $(\lambda_{h_1})_{\text{cap}} < 0$; this indicates that Marangoni stresses exert a destabilizing influence, while capillarity, which is proportional to $\mathscr{C}$, is stabilizing.
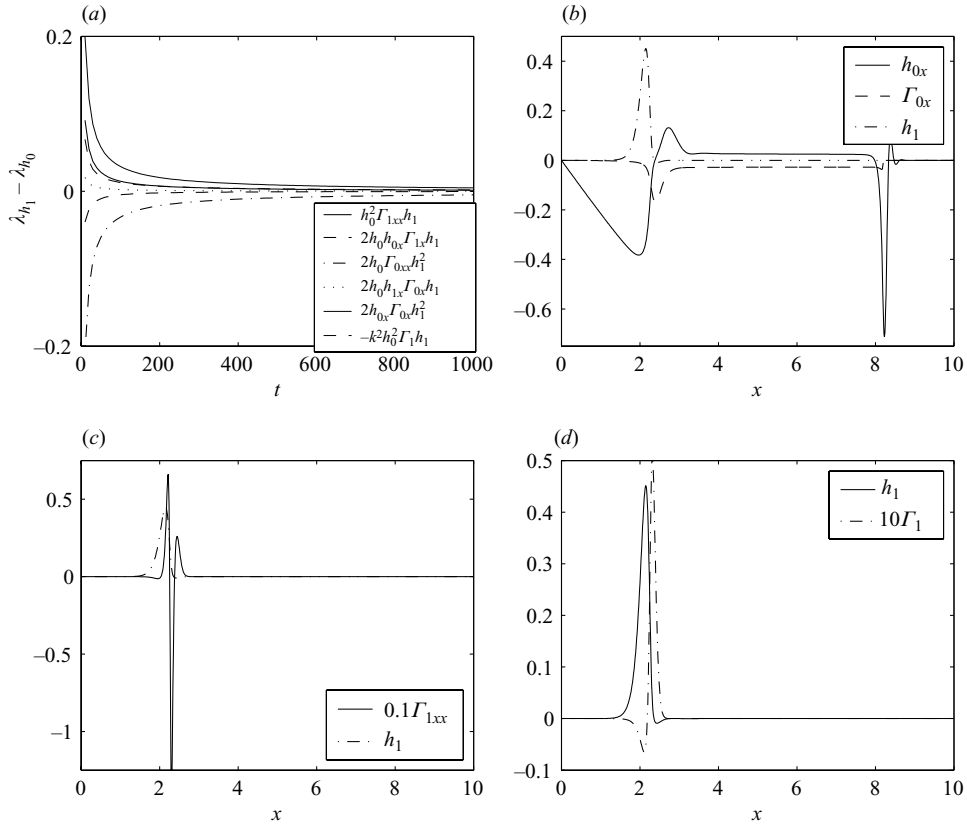
FIGURE 15. (*a*) Decomposition of the instantaneous growth rate associated with Marangoni stresses, $(\lambda_{h_1})_{\mathrm{mara}}$; (*b–d*) numerical solutions of the constituents of the terms providing the three largest contributions to $(\lambda_{h_1})_{\mathrm{mara}}$ (see (*a*)), at $t = 500$. The parameter values are as in figure 14.

We then examine the temporal evolution of the individual contributions to $(\lambda_{h1})_{\mathrm{mara}}$ in order to further isolate the reasons for unstable flow; these are shown in figure 15. As is clearly seen from figure 15(*a*), the integral of the term $2h_{0x}\Gamma_{0x}h_1^2$, a component of the perturbed streamwise Marangoni flow, over the spatial domain represents the largest positive, and therefore destabilizing, contribution to $(\lambda_{h_1})_{\mathrm{mara}}$ over the time duration investigated. As an aside, for the nonlinear equation of state we can now interpret the rather weak initial growth shown in figure 12(*g,h*), for strong nonlinearity, as being due to the dominant growth term that contains $-\sigma_\Gamma(\Gamma_0)\Gamma_{0x}$; the gradient of $\sigma$ is, from figure 4, small over the range of $\Gamma$ present in the thinned region at those times. Examination of the numerical solutions for the constituents of $2h_{0x}\Gamma_{0x}h_1^2$, which are $h_{0x}$, $\Gamma_{0x}$, $h_1$, presented in figure 15(*b*), shows that instability is promoted by steeper deposition and surfactant concentration slopes, that is by an increase in mobility, in the region of adjustment onto the thin liquid layer downstream. Factors that lead to larger $|h_{0x}|$ and $|\Gamma_{0x}|$, such as, for instance, smaller values of $b$ or larger $Pe$ will therefore ultimately lead to more unstable flow characterized by smaller onset times and patterns of smaller wavelength. It is interesting to note that the analogous term in thermally driven dynamic contact lines is also the largest contributor to unstable flow and finger formation (Kataoka & Troian 1997).

Other destabilizing contributions come from another component of the perturbed streamwise Marangoni flow, the $h_0^2 h_1 \Gamma_{1xx}$ term, and the transverse Marangoni flow term, $-k^2 h_0^2 \Gamma_1 h_1$; numerical solutions of their constituents are shown in figures 15(*c*) and 15(*d*), respectively. Inspection of figure 15(*d*) shows that positive-$h_1$ and negative-$\Gamma_1$ regions coincide resulting in a destabilizing contribution. Note that this term has no analogue in the thermally driven fingering problem.

It is worthwhile attempting to construct a physical mechanism leading to a fingering instability. Let us imagine that, at the edge of the drop and just within the thinned region, we have a small periodic fluctuation in the height. The local increase, $h_1$ say, results in an increase in surface velocity of $h_1 \Gamma_{0x}$ and a consequent increase in the amount of surfactant advected from this region. This creates a local decrease in the surfactant concentration, as shown in figures 8(*d*) and 15(*d*), which clearly demonstrate that $h_1 \Gamma_1 < 0$ over a substantial extent of the thinning region. The local decrease in surfactant concentration leads to the advection of more surfactant and liquid into the region of local height increase, away from neighbouring thinned regions, via Marangoni stresses. This, in turn, leads to the formation of alternating relatively thick and thin fluid regions. The local increase in the height of the relatively thick regions and the relative deficiency in surfactant concentration therein, encourages fluid to flow into these thickened regions preferentially. As the contrast in the magnitude of the film thickness between transverse thick and thin region increases, the thicker regions, which are more mobile, spread relatively faster becoming more elongated and finger-like. The initial height discrepancy between the drop and the precursor is essential to this mechanism, a feature first correctly noted by Troian *et al.* (1990): the flow on a thinner precursor is more efficient at trapping surfactant within the drop, leading to more severe local thinning, which 'pins' the disturbances preventing them from being convected away and leading to their local amplification.

### 3.3.3. *Quasi-steady-state approximation (QSSA)*

We have also examined the stability of the spreading process in the quasi-stead-state approximation (QSSA). The base state profiles are frozen at a time, $t_f$, and their stability characteristics are then determined via solution of equations (2.11) and (2.12) as an initial value problem. The quasi-static growth rates, $\lambda_{qssa}$, of applied disturbances of wavenumber $k$, which are parameterized by $t_f$, are then extracted.

Figure 16(*a*) shows numerically constructed dispersion curves for $t_f = 100, 200$ and $400$ with $b = 0.1$, $\mathscr{C} = 10^{-3}$, $\alpha \to \infty$ and $Pe = 10^5$, while figure 16(*b*) examines the effect of $b$ on these curves with the other parameters held constant. These dispersion curves exhibit a well-defined 'most dangerous' mode, $k_m$, at intermediate $k$ values and a large $k$ 'cut-off' mode, $k_c$. These results also clearly show that increasing $t_f$ and $b$ is stabilizing, characterized by a shift of both $k_m$ and $k_c$ towards lower $k$ values and an overall decrease in the magnitude of the growth rates. The dependence on $b$ shown in figure 16(*b*) is in agreement with the results of the transient growth analysis (TGA) of the evolving base state discussed previously and further underscores the significance of having a large thickness contrast for the instability to occur. The dependence on $t_f$ is also in agreement with the results shown in figure 14: the decrease in growth rate is due to the relaxation of the surfactant concentration and film thickness gradients with time, which provide the driving force for the instability. This is reminiscent of the QSSA study of miscible viscous fingering (Tan & Homsy 1986): the magnitude of $\lambda_{qssa}$ decreases as that of the concentration gradient of the less viscous fluid decays with $t_f$. We have also checked that the effects of $\mathscr{C}$ and $Pe$ on $\lambda_{qssa}$ are in agreement with the trends predicted by the TGA.
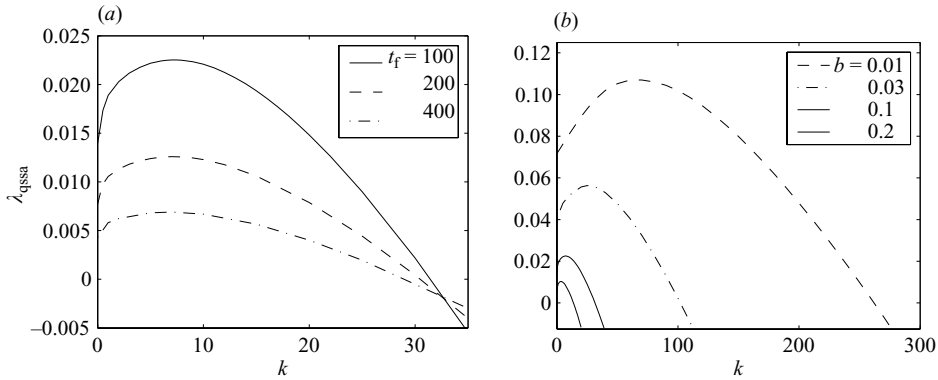
FIGURE 16. Stability of a 'frozen' base state in the quasi-steady-state approximation. (*a*) Dispersion curves showing the effect of $t_f$ with $t_f = 100, 200, 400$ and $b = 0.1$. (*b*) Effect of $b$ on the dispersion curves with $t_f = 100$, $\alpha \to \infty$, $\mathscr{C} = 10^{-3}$ and $Pe = 10^5$.

Examination of the linear stability of the system only predicts the conditions necessary for unstable flow at the onset of instability. To study the nonlinear stability of the spreading process the fully nonlinear, two-dimensional governing equations, (2.5) and (2.6), must be solved. Results from these numerical simulations are presented next.

### 3.4. *Two-dimensional numerical simulations*

In this section, we examine the stability of the spreading process in the nonlinear regime using the ADI (alternating direction implicit) scheme described in detail in the Appendix. ADI methods and their operator-splitting cousins are the method of choice among practitioners solving the thin-layer fluid equations that contain capillarity terms. For instance, Eres, Schwartz & Roy (2000) successfully utilize this method for a related fingering process. There is a notable difference, however, in that we have a mobile surfactant species that is absent from other studies.

The principal idea is described in Press *et al.* (1986) and illustrated there for the heat equation. One aims to produce a Crank–Nicholson-like set of equations that deal with each space direction independently and still produces a consistent (low order in time) scheme. For nonlinear capillary thin-film equations, a discussion is given by Schwartz (1998) and Witelski & Bowen (2003). The main advantage is that two-dimensional implicit, or semi-implicit, calculations are done via one-dimensional computations; as matrix inversion is involved the computational savings are enormous. It is vital to use semi-implicit schemes as, after spatial discretization, the governing system of ODEs for the discretized nonlinear surfactant equations is stiff; if one uses central difference approximations for the spatial derivatives then the matrices to invert are tri- or penta-diagonal (cyclic if periodicity is invoked) and sparse inversion routines can then be employed. The upshot is that one can construct highly accurate, and reasonably fast, schemes in this manner. The full details of the scheme are relegated to the Appendix.

Two-dimensional numerical solutions are obtained starting from

$$\left.\begin{aligned}
h(x, y, 0) &= (1 - x^2 + b)H(1 - x) + bH(x - 1) + A \exp\left(-\mathrm{B}(x - 1)^2\right) \sum_{i=1}^{N} C_i \cos(k_i y), \\
\Gamma(x, y, 0) &= H(1 - x),
\end{aligned}\right\}$$

$$(3.7)$$

where $A \in (10^{-3}\text{--}10^{-2})$, $B = 5$, $1 \leqslant N \leqslant 4$, $k_i \leqslant 20$ and $C_i \sim O(1)$. These initial conditions correspond to finite-amplitude perturbations consisting of several transverse modes that are localized at the edge of the surfactant deposition. This allows us to draw comparisons with the TGA and examine trends. Later in this section, we also initiate numerical simulations without the cosines and have the amplitudes of the perturbation chosen randomly from a uniform distribution on $[-0.01, 0.01]$; this is more representative of an experiment.

The two-dimensional simulations are performed on a grid $0 < x < L_x$, $0 < y < L_y$ and are subject to the following boundary conditions:

$$h_x(0, y, t) = h_{xxx}(0, y, t) = 0, \quad h(L_x, y, t) = b, \quad h_x(L_x, y, t) = 0, \\ \Gamma_x(0, y, t) = 0, \quad \Gamma(L_x, y, t) = 0. \tag{3.8}$$

Periodic boundary conditions are also imposed along the edges of the grid at $y = 0, L_y$. Typically we utilize a $2\pi$ square grid and have a $200 \times 200$ mesh. We have ensured that the two-dimensional solutions in the absence of applied perturbations are in precise agreement with the one-dimensional solutions obtained using EPDCOL, and with axisymmetric solutions. It is also possible to connect these computations with the TGA analysis: the 'energies' defined for the transient growth analysis $E_{h_1}$, $E_{\Gamma_1}$ have two-dimensional analogues

$$E_{h_1} = \frac{k}{\pi} \int_{-\pi/k}^{\pi/k} \int_0^{\infty} [h(x, y, t) - h_0(x, t)]^2 \, \mathrm{d}x \, \mathrm{d}y, \tag{3.9}$$

and similarly for the surfactant 'energy'.

In figure 17 we show some results from a computation forced by a single wave-number disturbance and we fix typical parameters, $k = 6$, $\mathscr{C} = 10^{-4}$, $b = 0.1$, $\alpha \to \infty$ and $Pe = 10^4$; the initial amplitude of the perturbation is $10^{-2}$. Shown in this figure is the time evolution of $E_{h_1}$ calculated using TGA, initiated by a height perturbation of the same form, and from the fully nonlinear two-dimensional simulations. The perturbations from the TGA plotted as $h_1(x, t) \cos ky$ are shown in the figure, as is the difference of the computed two-dimensional simulation from the base state. This gives us confidence both in the TGA, as an accurate interpretation of the flow, and in the two-dimensional numerical scheme.

We neglect nonlinearities in (2.1) by setting $\alpha \to \infty$ and use a linear equation of state. Figures 18 and 19 show surface and contour plots of the film thickness, $h(x, y, t)$, at $t = 5, 25, 50, 100$, generated with $b = 0.05$, $\mathscr{C} = 10^{-4}$ and $Pe = 10^4$; the contours are graduated in steps of $1/15$. These solutions were obtained starting from an initial condition given by equations (3.7) with $N = 4$, $A = 0.01$, $B = 5$, $C_1 = C_2 = C_3 = 1$, $C_4 = 0.5$, $k_1 = 2$, $k_2 = 5$, $k_3 = 7$ and $k_4 = 20$. This initial condition represents a combination of small- and large-wavenumber disturbances, that, as shown in figures 7 and 10, dominate the spreading at early and late times, respectively. The results at $t = 5$, and, to a lesser extent, at $t = 25$, show weak undulations along and behind the leading front, which decay and eventually disappear. These are the transient growth and decay modes found in the absence of the precursor/drop height mismatch; they are irrelevant to the growth in the thinning region.

Of much more interest is the behaviour at the edge of the drop, in the thinning region, in which very pronounced and striking fingering patterns emerge. The rounder low-wavenumber disturbances appear to split readily, and the higher wavenumber disturbances lengthen to form distinctive fingers (see for instance the upper two fingers at $t = 100$ in figures 18 and 19 that have emerged from a thicker initial undulation).
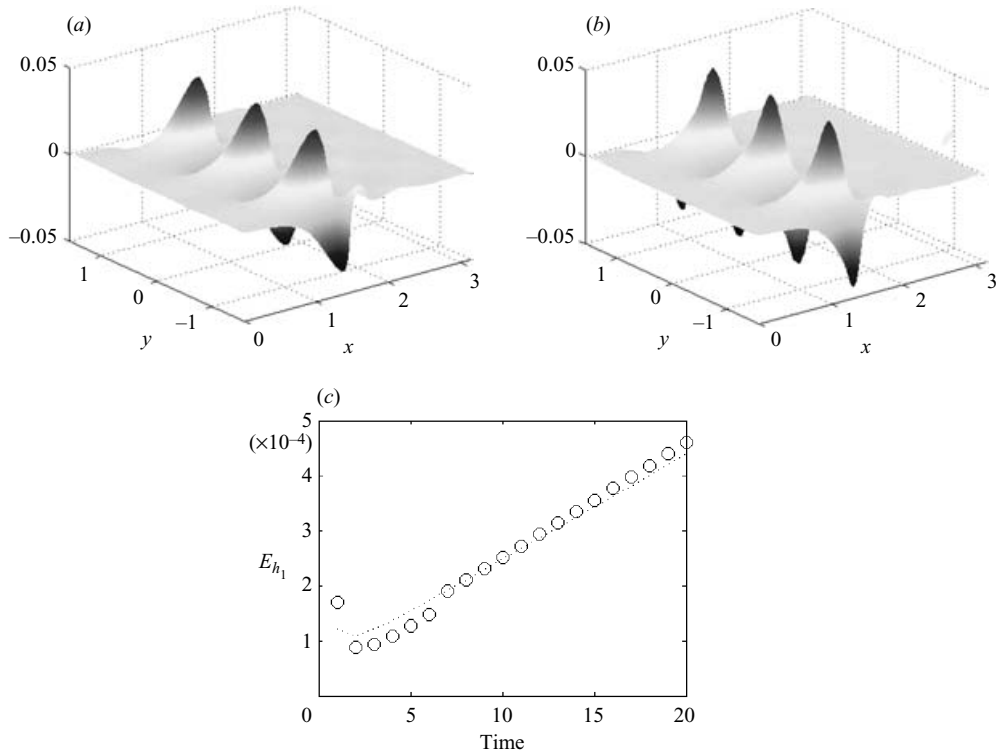
FIGURE 17. (*a*, *b*) The height perturbations from the TGA and fully two-dimensional simulations respectively at $t = 20$. (*c*) The 'energies' calculated using TGA (dotted) and two-dimensional simulations (circles). The parameter values are $k = 6$, $\mathscr{C} = 10^{-4}$, $b = 0.1$, $Pe = 10^4$ and $\alpha \to \infty$.

The fingers appear to steepen at their leading edge with increasing time, a feature also reported by Eres *et al.* (2000) who conducted two-dimensional numerical simulations of surface-shear-stress-driven films (in the absence of surfactant). Finger 'shielding' is also evident, an example of which can be seen by inspection of the $5 < y < 2\pi$ region in the contour plot associated with $t = 100$ in figure 19. Here, the third finger from the top has ceased moving: it is effectively shielded by the longer evolving fingers to the sides. In these cases, fluid is preferentially channelled into the moving longer fingers. Thus fully two-dimensional simulations evidently show features observed in the experiments of Troian *et al.* (1989) and Afsar-Siddiqui *et al.* (2003*a*), for instance, conducted on film thicknesses in the approximate range of 0.1–1 μm and 0.25–200 μm, respectively. It should be mentioned, however, that the level of finger branching increases with surfactant solubility (Afsar-Siddiqui *et al.* 2003*b*).

Figure 20 shows the surfactant concentration decreasing slightly and localized along the positions of the fingers, and rising marginally ahead of them. Also shown in figure 20 is a section across the fingers at an earlier time, $t = 25$, through $x = 1.25$, 1.55 that shows the difference of the height and (10×) surfactant values from their base state values; the decrease (increase) of surfactant at peaks (troughs) of the height perturbation is evident for the slice across the fingers (panel *b*). It is notable that the magnitude of the deviation from the surfactant base state solution is relatively small in that region, in agreement with the results of the TGA, which also showed
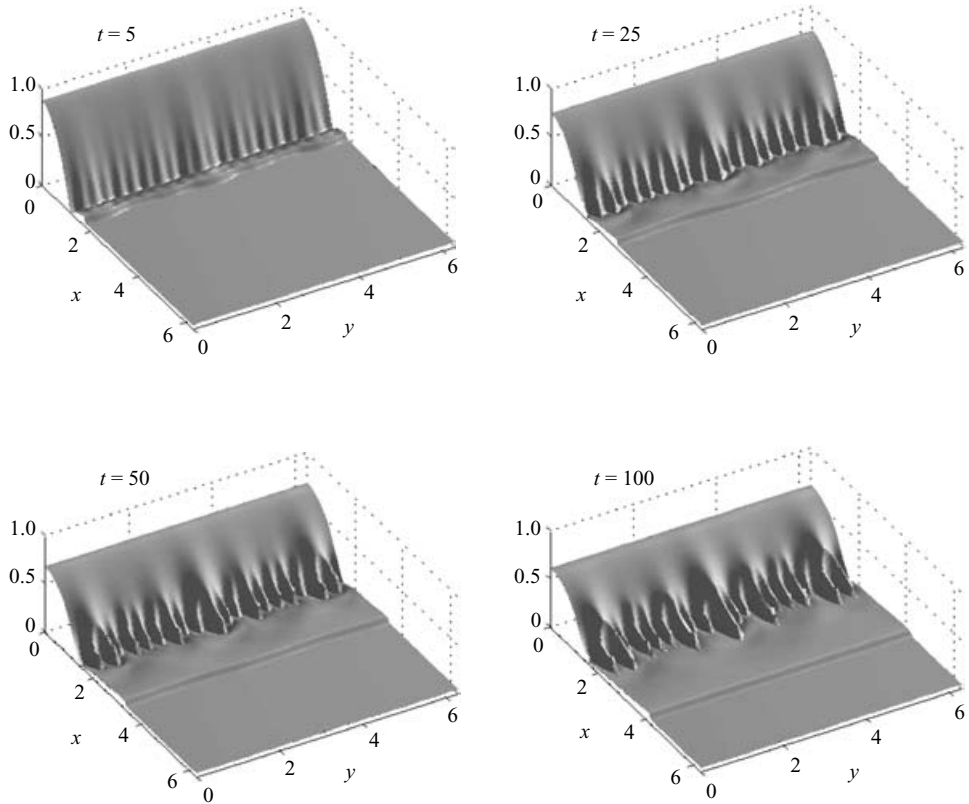
FIGURE 18. Surface plots of the film thickness, $h(x, y, t)$, showing the onset and evolution of the fingering patterns, generated with $Pe = 10^4$, $\mathcal{C} = 10^{-4}$, $b = 0.05$, $\alpha \to \infty$, $N = 4$, $A = 0.01$, $B = 5$, $C_1 = C_2 = C_3 = 1$, $C_4 = 0.5$, $k_1 = 2$, $k_2 = 5$, $k_3 = 7$ and $k_4 = 20$.

the magnitude of $h_1$ to far exceed that of $\Gamma_1$ there (see, for instance, figures 8 and 14). However, just ahead of the fingers in figure 20(c) we note that the surfactant concentration rises, in agreement both with the mechanism that we propose and with the TGA simulations.

Next we examine the effect of varying the precursor-droplet height ratio, $b$, on the fingering patterns in the nonlinear regime. Figure 21 shows the height field at a fixed time $t = 25$, for different $b$ values. Inspection of this figure reveals that increasing $b$ leads to faster propagation of the surfactant leading edges with a concomitant reduction in the degree of thinning upstream, at the drop leading edge; this was also evident in figure 6(a, b). Consequently, the fingering patterns, which are barely discernible at $b = 0.75$, become increasingly pronounced with decreasing $b$, entirely in line with the TGA predictions.

The results presented so far correspond to numerical solutions starting from smooth, regular and symmetric initial conditions. In an effort to capture nonlinear events observed experimentally, however, we perform 'numerical experiments' by conducting simulations starting from the following initial condition:

$$\left.\begin{aligned} h(x, y, 0) &= (1 - x^2 + b)H(1 - x) + bH(x - 1) + A(y)\exp(-5(x - 1)^2), \\ \Gamma(x, y, 0) &= H(1 - x). \end{aligned}\right\} \tag{3.10}$$
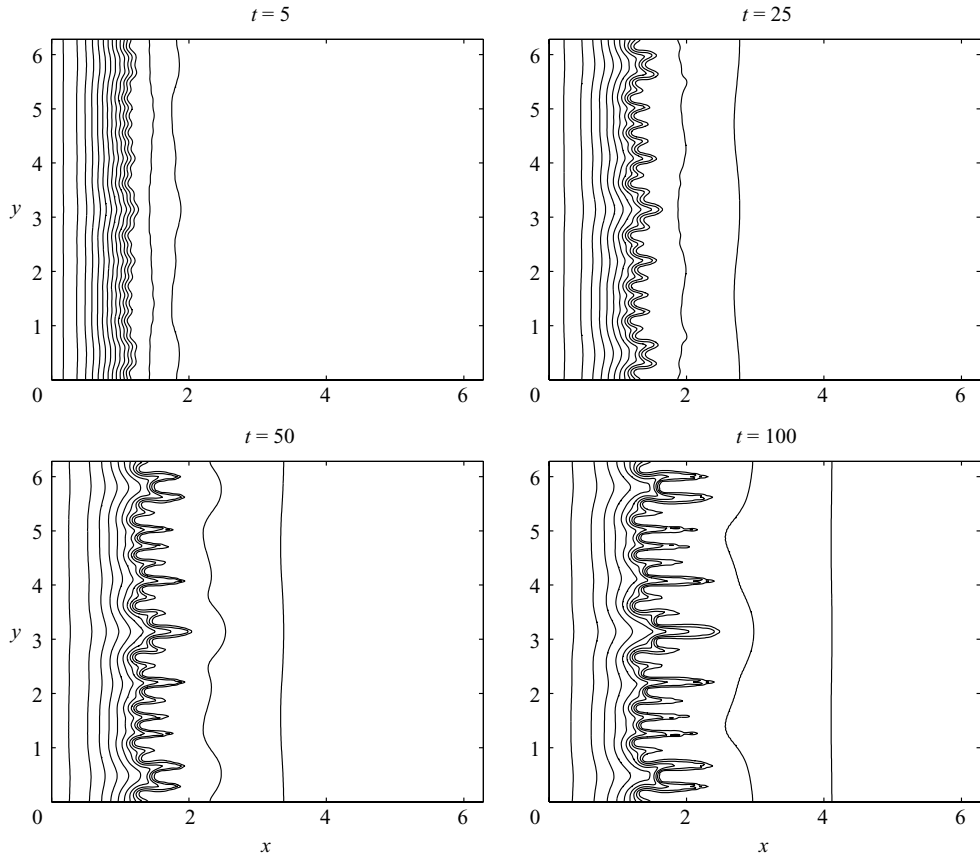
FIGURE 19. Contour plots of $h(x, y, t)$, (the contours show changes in height of 1/15) for the same parameters and times as those in figure 18.
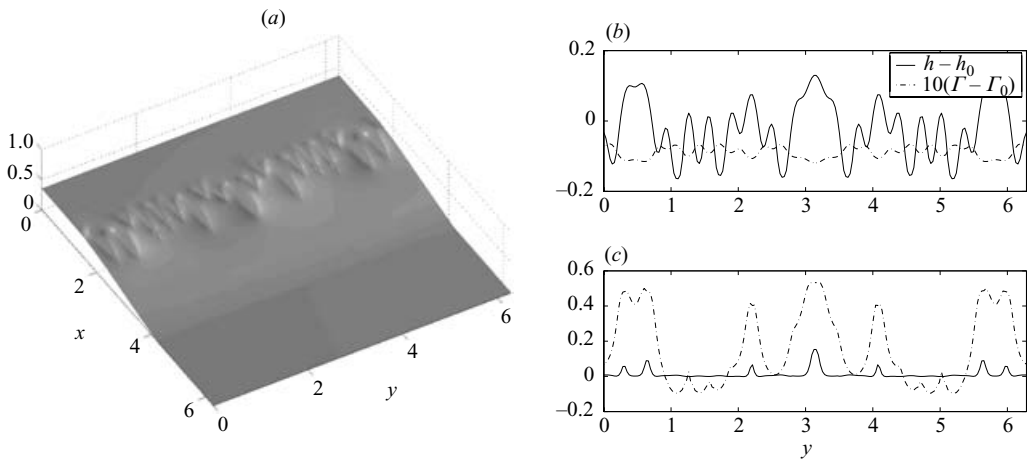


FIGURE 20. (*a*) A surface plot of the surfactant concentration, $\Gamma(x, y, t)$, at $t = 100$ and the same parameters as in figure 18. (*b*) For $t = 25$, a cross-section across the fingers (at $x = 1.25$) and (*c*) just ahead of the fingers (at $x = 1.55$) showing the height and $(10\times)$ surfactant differences from the base state.
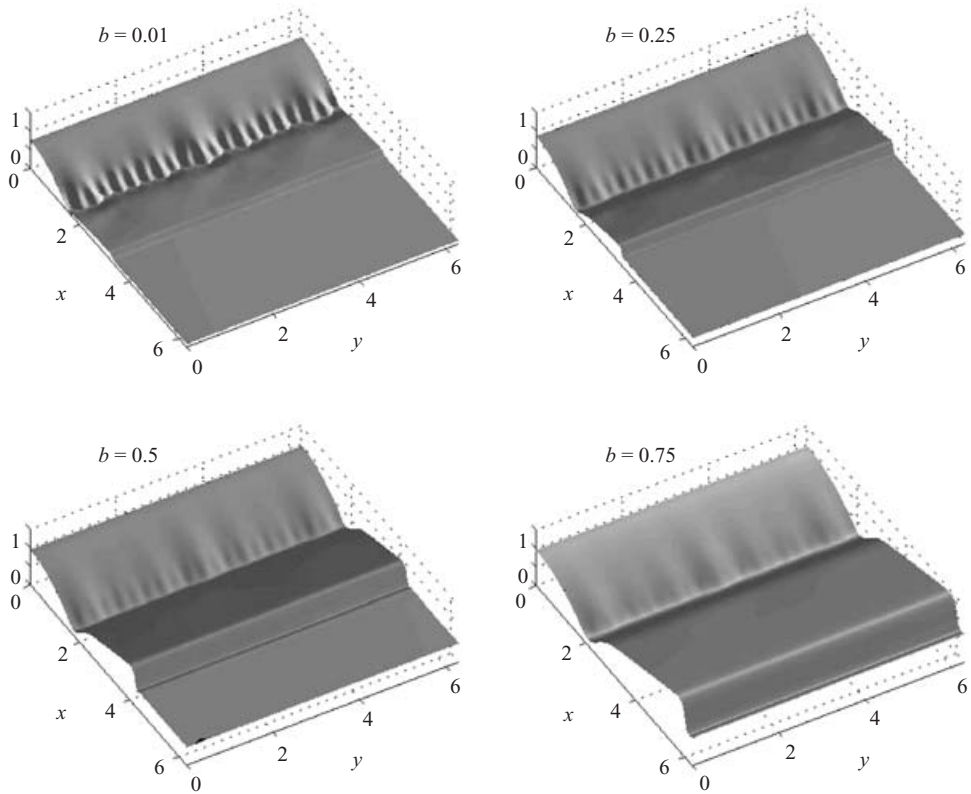
FIGURE 21. The effect of varying $b$ on the observed fingering pattens: surface plots of $h(x, y, t)$ for $b = 0.1$, $b = 0.25$, $b = 0.5$ and $b = 0.75$ at $t = 25$. The rest of the parameters and the initial condition are as in figure 18.

Here, the $A(y)$ are random values chosen from a uniform distribution on $[-0.01, 0.01]$. As shown in figure 22, the initially noisy disturbances rapidly organize into coherent structures and fingering patterns readily emerge. Loss of symmetry, competition between fingers and nonlinear interactions are also clearly seen in figure 23 which is for the lower precursor-drop depth ratio of $b = 0.05$. It is interesting to see in figure 23(b) that thicker protuberances have split into thinner fingers that interact with some fingers that elongate at the expense of others. These long thin rivulet-like fingers then appear to undergo a Rayleigh-type instability, which targets sufficiently long threads. This is reminiscent of the droplet formation shown by Eres *et al.* (2000) to accompany the later stages of the fingering process in surface-shear-stress-driven flows.

The wavelength selection mechanism in the nonlinear regime results from a competition between such processes as tip-splitting, coalescence and shielding. Nevertheless, it may be expected that the results of the linear analyses presented previously and the present nonlinear simulations will be in agreement at relatively early times, beyond which noisy disturbances have been filtered through the linear mechanisms resulting in the emergence of the wavenumber associated with the most dangerous linear mode, $k_m$. In order to identify the value of $k_m$, we have plotted the power spectrum of the difference between the film thickness surface and the
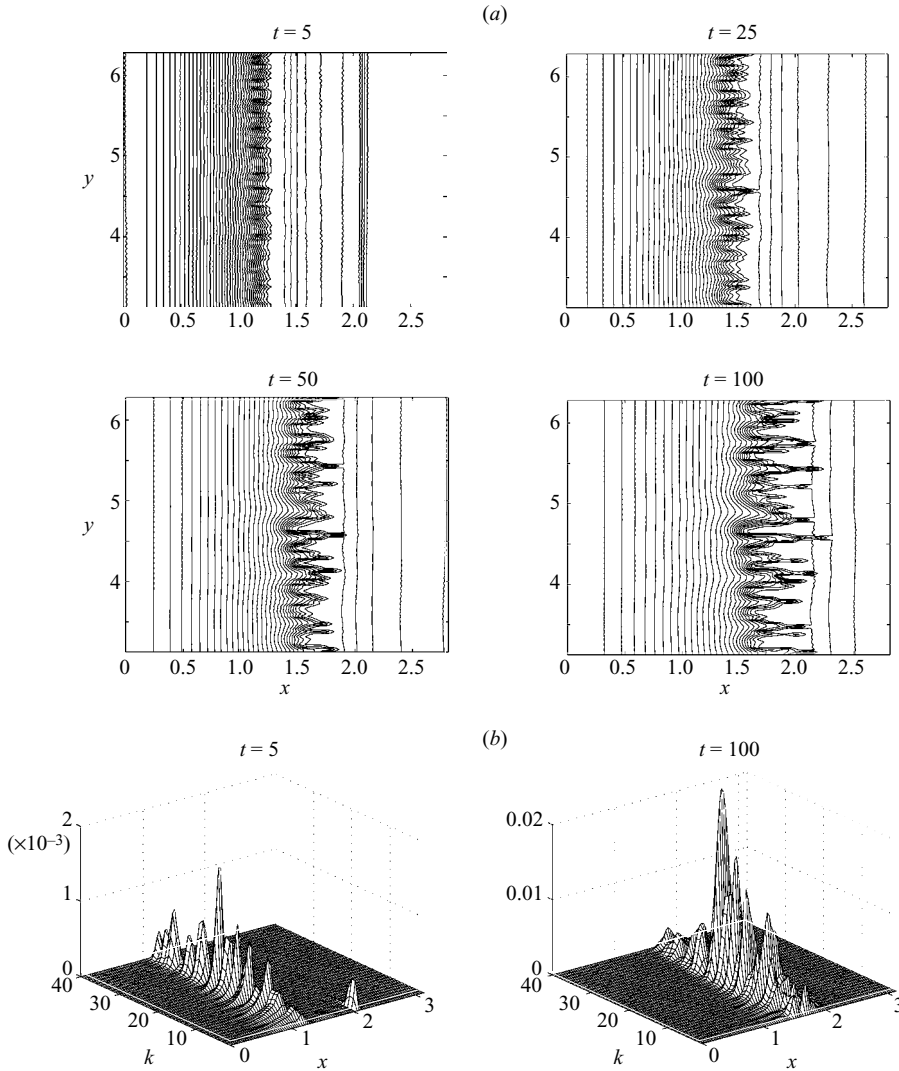
FIGURE 22. Wavelength selection in the nonlinear regime. (*a*) Evolution of the disturbances shown as contour plots of $h(x, y, t)$ for $b = 0.1$ at $t = 5, 25, 50, 100$, initiated with random perturbations in the film thickness described by (3.10). (*b*) The power spectrum of the film thickness difference from the base state at $t = 5, 100$ showing a maximal value at $k = 24$ localized in the thinning region; at $t = 5$ there is a minor low-wavelength disturbance at the leading front. The rest of the parameters are as in figure 18.

unperturbed base state. This is obtained using the FFT in the $y$-direction using Matlab for $b = 0.1$ and the same parameters as in figure 18; this is shown in figure 22 for $t = 5$ and $t = 100$. Inspection of this figure shows that a dominant wavenumber of $k \sim 24$ can be identified, which is in line with the TGA predictions of figure 7. The computations here are for slightly different values of $Pe$ ($\mathscr{C}$); however, the TGA results in figure 12 show that the growth rates are insensitive to these parameters at such large (small) values. Note also that at $t = 5$ a small low-wavenumber disturbance can be identified at the leading front, which rapidly decays.
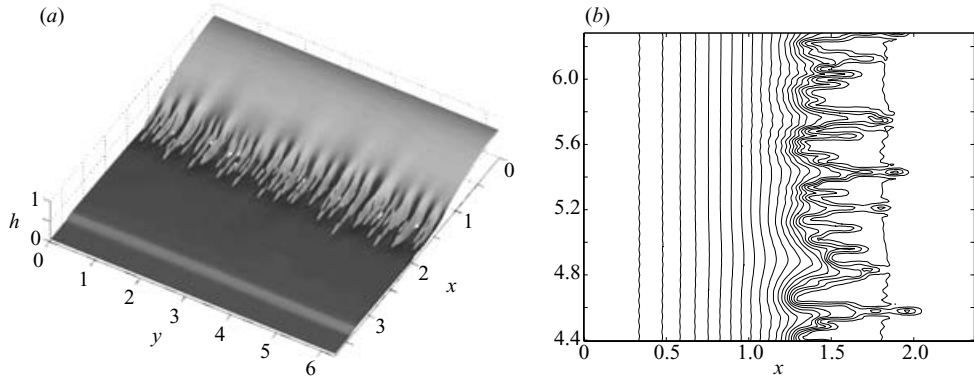
FIGURE 23. Surface plot of $h(x, y, t)$, shown in (a), at $t = 50$ with $b = 0.05$ and the other parameters remaining unaltered from figure 18, however, the initial conditions correspond to essentially random perturbations, described by Eq. (3.10). Panel (b) shows a contour plot of a subsection of the surface plot shown in (a).

## 4. Conclusions

The stability of the spreading of an insoluble surfactant deposition on the surface of a thin liquid layer has been investigated using a coupled system of two-dimensional evolution equations, for the film thickness and surfactant concentration, derived using lubrication theory. The equations are parameterized by the ratio of the maximal deposition height and the thickness of the precursor film, $b$, a capillarity parameter, $\mathscr{C}$, a surfactant equation-of-state nonlinearity parameter, $\alpha$, and the surface Péclet number, $Pe$.

A transient growth analysis of the evolving one-dimensional base state was conducted, which revealed growth of linear disturbances. Inspection of the temporal evolution of the normalized disturbance energy showed that after a short initial period of time, a perturbation of intermediate wavenumber is selected, which becomes 'pinned' in the 'contact' region. A subsequent decomposition of the instantaneous disturbance growth rate showed that Marangoni stresses are primarily responsible for the instability, with capillarity and surface diffusion providing a large-wavenumber cut-off. A parametric investigation, which used the normalized disturbance energy as a basis, also showed that unstable flow is promoted by a decrease in $b$ and $\mathscr{C}$ and an increase in $Pe$. A detailed examination of the destabilizing terms in the governing equations revealed that factors promoting an increase in the magnitude of the base state deposition and surfactant concentration slopes in the contact region (such as decreasing $b$ and increasing $Pe$, for instance) are destabilizing. The growth rate saturates for typical values of the Péclet and capillary parameters, which are large and small, respectively. Hence, these parameters are of subsidiary importance to the geometric parameter $b$. A nonlinear equation of state appears not to be essential for the finger growth mechanism that we describe. Nonetheless, we have investigated its effect on the instability briefly and demonstrated that disturbance growth can be maximized over a range of small $\alpha$ values, which correspond to a highly nonlinear equation of state, representative of high surfactant concentrations.

We have also investigated the stability of the spreading process in the quasi-steady-state approximation, which assumed that the rate of change of the perturbations far exceeds that of the base state. The stability of base state profiles 'frozen' at a time $t_f$ to transverse disturbances were then analysed and growth rates as a function

of disturbance wavenumber were plotted. These numerically generated dispersion curves exhibit well-defined 'most dangerous' and 'cut-off' modes, indicative of mode selection in the linear regime. The magnitude of the quasi-static growth rate was found to decrease as a function of $t_f$ as both the base state and surfactant concentration gradients relaxed to smaller values.

Finally, transient direct numerical simulations of the fully nonlinear two-dimensional governing equations were performed starting from a multi-cosine-mode initial condition as well as pseudo-random perturbations of the film thickness. Inspection of contour and surface plots from that study revealed the formation of fingering patterns in the contact region, which spread behind the advancing thickened front of the precursor film at the surfactant leading edge. The results of the simulations, which were initiated with random disturbances, showed the rapid organization of the perturbations into coherent structures at relatively early times. This was then followed by nonlinear interactions between adjacent fingers, tip-splitting and shielding. It must be mentioned, however, that these features are more reminiscent of the experimental observations of Troian *et al.* (1989) on thin films and sparingly soluble surfactant and the work of Afsar-Siddiqui *et al.* (2003*b*), which involves soluble surfactant on thicker films. Future work will focus on extending the present work to cover surfactant solubility effects.

In summary, the main finding of the present work is the determination of a physical scenario that gives rise to sustained fingering behind the surfactant leading edge during the spreading process; this does not involve van der Waals interactions. Previous authors had either found transient growth followed by decay in the absence of van der Waals interactions (Matar & Troian 1999*a*), or sustained finger-like protrusions in the thinning region in the presence of these forces (Matar & Troian 1999*b*; Warner *et al.* 2002). These studies modelled the spreading of a surfactant monolayer of negligible thickness on the surface of a thin film of uniform height. As demonstrated here, the inclusion of the disparity in thickness between the deposited surfactant drop and underlying film is an essential ingredient for fingered spreading.

## Appendix. Numerical techniques in two dimensions

Considering the governing equations (2.5), (2.6), we note that there are two sources of numerical difficulty: the nonlinear high-order terms $\mathscr{C}\nabla\cdot h^3\nabla\nabla^2 h$ and the surface diffusion $\nabla^2\Gamma/Pe$ in the $h$ and $\Gamma$ evolution equations, respectively. We choose to treat these awkward terms semi-implicitly: a fully explicit two-dimensional spectral solver using adaptive Runge–Kutta time stepping requires time steps several orders of magnitude smaller in order to control these terms. That spectral scheme is used to cross-verify the ADI code (it is also checked versus axisymmetric and one-dimensional computations).

We introduce the following operators:

$$\mathscr{L}_x^H = \left[I + \frac{C}{6}\Delta t\frac{\partial}{\partial x}\left(h^3\frac{\partial^3}{\partial x^3}\right)\right], \quad \mathscr{L}_x^\Gamma = \left(I - \frac{1}{2Pe}\Delta t\frac{\partial^2}{\partial x^2}\right),$$

where $\mathscr{L}_y^H, \mathscr{L}_y^\Gamma$ are identical, but with $y$ replacing $x$. We aim, at least initially, for a first-order scheme in time, so $h_t = [h^{n+1} - h^n]/\Delta t + O(\Delta t)$ with $h^n$ as the value of $h$ at $t = t^n$, and $\Delta t$ as the time step. The nonlinear terms in $\mathscr{L}_{x,y}^H$ are evaluated at $t = t^n$. Treating the advection terms explicitly, and adopting a Crank–Nicholson-like approach to the awkward terms, gives

$$\frac{\left[h^{(n+1)} - h^{(n)}\right]}{\Delta t} = -\nabla \cdot \left(\frac{h^2}{2}\nabla\sigma\right)^{(n)} - \frac{C}{6}\nabla \cdot (h^3\nabla\nabla^2 h)^{(n+1)} - \frac{C}{6}\nabla \cdot (h^3\nabla\nabla^2 h)^{(n)},$$

$$\frac{\left[\Gamma^{(n+1)} - \Gamma^{(n)}\right]}{\Delta t} = \frac{1}{2Pe}\nabla^2\Gamma^{(n+1)} + \frac{1}{2Pe}\nabla^2\Gamma^{(n)} - \nabla \cdot \left(\Gamma h\nabla\sigma + \frac{C}{2}\Gamma h^2\nabla\nabla^2 h\right)^{(n)}.$$

Keeping in mind the low order in time of our proposed scheme, one can reduce it to

$$\mathscr{L}_x^H q^H = \mathscr{L}_x^H \mathscr{L}_y^H \left(h^{(n+1)} - h^{(n)}\right) = -\Delta t \left[\nabla \cdot \left(\frac{h^2}{2}\nabla\sigma\right) + \frac{C}{3}\nabla \cdot (h^3\nabla\nabla^2 h)\right]^{(n)} + O(\Delta t)^2,$$

$$\mathscr{L}_x^H q^\Gamma = \mathscr{L}_x^\Gamma \mathscr{L}_y^\Gamma \left(\Gamma^{(n+1)} - \Gamma^{(n)}\right) = \Delta t \left[\frac{1}{Pe}\nabla^2\Gamma - \nabla \cdot \left(\Gamma h\nabla\sigma + \frac{C}{2}\Gamma h^2\nabla\nabla^2 h\right)\right]^{(n)} + O(\Delta t)^2.$$

The left-hand terms are products of operators only in $x$ or $y$ so dummy variables $q^H, q^\Gamma$ are introduced that satisfy $\mathscr{L}_y^H(h^{(n+1)} - h^{(n)}) = q^H$ and $\mathscr{L}_y^\Gamma(\Gamma^{(n+1)} - \Gamma^{(n)}) = q^\Gamma$. One first solves a one-dimensional problem in $x$, and then in $y$. For further details of the ADI methodology Marchuk (1990) provides a lengthy introduction and the recent article by Witelski & Bowen (2003) compares variants of the method for capillary thin-film equations. One can partially overcome the low order in time issue by adopting Richardson extrapolation. However in practical terms one appears to be limited by stability issues that require small time steps of the order $10^{-5}$ to be used.

For the computations in the text we utilize a domain $0 < x < 2\pi$ and $0 < y < 2\pi$ and apply periodic boundary conditions along $y = 0, 2\pi$ and Neumann boundary conditions along $x = 0, 2\pi$. The operators $\mathscr{L}_{x,y}$ and $h, \Gamma$ are discretized in space, the resulting sparse matrices are banded for $\mathscr{L}_x$ and cyclic banded for $\mathscr{L}_y$; the latter are dealt with using the Woodbury formulae (Press *et al.* 1986). Alternatively conjugate gradient style iterative methods can be, and were, utilized; however, there appeared to be no advantage in terms of speed or accuracy.

## REFERENCES

AFSAR-SIDDIQUI, A. B., LUCKHAM, P. F. & MATAR, O. K. 2003*a* Unstable spreading of an anionic surfactant on liquid films. Part I: Sparingly soluble surfactant. *Langmuir* **19**, 696–702.

AFSAR-SIDDIQUI, A. B., LUCKHAM, P. F. & MATAR, O. K. 2003*b* Unstable spreading of an anionic surfactant on liquid films. Part II: Highly soluble surfactant. *Langmuir* **19**, 703–708.

BARDON, S., CACHILE, M., CAZABAT, A. M., FANTON, X. & VILLETTE, S. 1996 Structure and dynamics of liquid films on solid surfaces. *Farad. Disc.* **104**, 307–316.

BORGAS, M. S. & GROTBERG, J. B. 1988 Monolayer flow on a thin film. *J. Fluid Mech.* **193**, 151–170.

BRAUN, R. J., SNOW, S. A. & PERNISZ, U. C. 1999 Gravitational drainage of a tangentially-immobile thick film. *J. Colloid Interface Sci.* **219**, 225–240.

CACHILE, M. & CAZABAT, A. M. 1999 Spontaneous spreading of surfactant solutions on hydrophilic surfaces:cnem in ethylene and diethylene glycol. *Langmuir* **15**, 1515–1521.

CACHILE, M., CAZABAT, A. M., BARDON, S., VALIGNAT, M. P. & VADENBROUCK, F. 1999 Spontaneous spreading of surfactant solutions on hydrophilic surfaces. *Colloids Surf.* A **159**, 47–56.

CACHILE, M., SCHNEEMLICH, M., HAMRAOUI, A. & CAZABAT, A. M. 2002 Films driven by surface tension gradients. *Adv. Colloid Interface Sci.* **96**, 59–74.

CRASTER, R. V. & MATAR, O. K. 2000 Surfactant transport on mucus films. *J. Fluid Mech.* **425**, 235–258.

DEWITT, A., GALLEZ, D. & CHRISTOV, C. 1994 Nonlinear evolution equations for thin liquid films with insoluble surfactants. *Phys. Fluids* **6**, 3256–3266.

DRAZIN, P. H. & REID, W. H. 1982 *Hydrodynamic Stability*. Cambridge University Press.

EDWARDS, D. A., BRENNER, H. & WASAN, D. T. 1991 *Interfacial Transport Processes and Rheology*. Butterworth-Heinemann.

ERES, M. H., SCHWARTZ, L. W. & ROY, R. V. 2000 Fingering phenomena for driven coating films. *Phys. Fluids* **12**, 1278–1295.

FISCHER, B. J. & TROIAN, S. M. 2003 Thinning and disturbance growth in liquid films mobilized by continuous surfactant delivery. *Phys. Fluids* **15**, 3837–3845.

FRANK, B. & GAROFF, S. 1995 Origins of the complex motion of advancing surfactant solutions. *Langmuir* **11**, 87–93.

GAVER III, D. P. & GROTBERG, J. B. 1990 The dynamics of a localized surfactant on a thin film. *J. Fluid Mech.* **213**, 127–148.

GAVER III, D. P. & GROTBERG, J. B. 1992 Droplet speading on a thin viscous film. *J. Fluid Mech.* **235**, 399–414.

GROTBERG, J. B. 1994 Pulmonary flow and transport phenomena. *Annu. Rev. Fluid Mech.* **26**, 529–571.

HALPERN, D. & GROTBERG, J. B. 1992 Dynamics and transport of a localized soluble surfactant on a thin film. *J. Fluid Mech.* **237**, 1–11.

HE, S. & KETTERSON, J. 1995 Surfactant driven spreading of a liquid on a vertical surface. *Phys. Fluids* **7**, 2640–2647.

JENSEN, O. E. & GROTBERG, J. B. 1992 Insoluble surfactant spreading on a thin viscous film: shock evolution and film rupture. *J. Fluid Mech.* **240**, 259–288.

JENSEN, O. E. & GROTBERG, J. B. 1993 The spreading of heat or soluble surfactant along a thin film. *Phys. Fluids* A **5**, 58–68.

KATAOKA, D. E. & TROIAN, S. M. 1997 A theoretical study of instabilities at the advancing front of thermally driven coating films. *J. Colloid Interface Sci.* **192**, 350–362.

KEAST, P. & MUIR, P. H. 1991 Algorithm 688 EPDCOL – a more efficient PDECOL code. *ACM Trans. Math. Software* **17**, 153–166.

LEENAARS, A. F., HUETHORST, J. A. M. & VAN OEKEL, J. J. 1990 Marangoni drying: A new extremely clean drying process. *Langmuir* **6**, 1701–1703.

MARCHUK, G. I. 1990 Splitting and alternating direction methods. In *Handbook of Numerical Analysis Vol 1* (ed. P. G. Ciarlet & J.-L. Lions), pp. 197–462. North Holland.

MARMUR, A. & LELAH, M. D. 1981 The spreading of aqueous surfactant solutions on glass. *Chem. Engng Commun.* **13**, 133–143.

MATAR, O. K. & CRASTER, R. V. 2001 Models for Marangoni drying. *Phys. Fluids* **13**, 1869–1883.

MATAR, O. K., CRASTER, R. V. & WARNER, M. R. E. 2002 Surfactant transport on highly viscous surface films. *J. Fluid Mech.* **466**, 85–111.

MATAR, O. K. & TROIAN, S. M. 1997 Linear stability analysis of an insoluble surfactant monolayer spreading on a thin liquid film. *Phys. Fluids* **9**, 3645–3657.

MATAR, O. K. & TROIAN, S. M. 1998 Growth of non-modal transient structures during the spreading of surfactant coated films. *Phys. Fluids* **10**, 1234–1237.

MATAR, O. K. & TROIAN, S. M. 1999*a* The development of transient fingering patterns during the spreading of surfactant coated films. *Phys. Fluids* **11**, 3232–3246.

MATAR, O. K. & TROIAN, S. M. 1999*b* Spreading of a surfactant monolayer on a thin liquid film: Onset and evolution of digitated structures. *Chaos* **9**, 141–153.

PRESS, W. H., FLANNERY, B. P., TEUKOLSKY, S. A. & VETTERLING, W. T. 1986 *Numerical Recipes: The Art of Scientific Computing*. Cambridge University Press.

RUSCHAK, K. J. 1978 Flow of a falling film into a pool. *AIChE J.* **24**, 705–709.

SAFFMAN, P. G. & TAYLOR, G. I. 1958 The penetration of a fluid into a porous medium or Hele-Shaw cell containing a more viscous liquid. *Proc. R. Soc. Lond.* A **245**, 312–329.

SCHWARTZ, L. W. 1998 Hysteretic effects in droplet motions on heterogeneous substrates: direct numerical simulation. *Langmuir* **14**, 3440–3453.

SCHWARTZ, L. W. & ROY, R. V. 2001 Some results concerning the potential energy of interfaces with nonuniformly distributed surfactant. *Phys. Fluids* **13**, 3089–3092.

SHELUDKO, A. 1967 Thin liquid films. *Adv. Colloid Interface Sci.* **1**, 391–464.

SHEN, S. F. 1961 Some considerations of the laminar stability of incompressible time-dependent basic flows. *J. Aerospace Sci.* **28**, 397–404.

SINCOVEC, R. F. & MADSEN, N. K. 1979 Algorithm 540 PDECOL. *ACM Trans. Math. Software* **5**, 326–351.

SPAID, M. & HOMSY, G. M. 1996 Stability of Newtonian and viscoelasticity dynamic contact lines. *Phys. Fluids* **8**, 460–478.

TAN, C. T. & HOMSY, G. M. 1986 Stability of miscible displacements in porous media: Rectilinear flow. *Phys. Fluids* **29**, 3549–3556.

TROIAN, S. M., HERBOHLZHEIMER, E. & SAFRAN, S. A. 1990 Model for the fingering instability of spreading surfactant drops. *Phys. Rev. Lett.* **65**, 333–336.

TROIAN, S. M., WU, X. L. & SAFRAN, S. A. 1989 Fingering instability in thin wetting films. *Phys. Rev. Lett* **62**, 1496–1499.

WARNER, M. R. E., CRASTER, R. V. & MATAR, O. K. 2002a Dewetting of ultrathin surfactant covered films. *Phys. Fluids* **14**, 4040–4054.

WARNER, M. R. E., CRASTER, R. V. & MATAR, O. K. 2002b Unstable van der Waals driven line rupture in Marangoni driven thin viscous films. *Phys. Fluids* **14**, 1642–1654.

WITELSKI, T. P. & BOWEN, M. 2003 ADI schemes for higher-order nonlinear diffusion equations. *Appl. Numer. Maths* **45**, 331–351.